

# PERTURB-*c*: Correlation Aware Perturbation Explainability for Regression Techniques to Understand Retrieval Black-boxes

Jools D. Clarke,<sup>1\*</sup> Gordon Yip<sup>2</sup> and Nikolaos Nikolaou<sup>1</sup>

<sup>1</sup>Department of Physics and Astronomy, University College London, Gower Street, WC1E 6BT London, United Kingdom

<sup>2</sup>NMES Faculty, King's College London, Strand Building, Strand, WC2R 2LS London, United Kingdom

Accepted XXX. Received YYY; in original form ZZZ

## ABSTRACT

In this paper we introduce *PERTURB-c*, a correlation-aware framework for interpreting black box regression models with one-dimensional structured inputs. We demonstrate this framework on a simulated case study with machine learning based transit spectroscopy retrievals of exoplanet WASP-107b. Characterising many exoplanet atmospheres can answer important questions about planetary populations, but traditional retrievals are very resource intensive; machine learning based methods offer a fast alternative however (i) they require high volumes data (only obtainable through simulations) to train and (ii) their complexity renders them black-boxes. Better understanding how they reach predictions can allow us to inspect for biases, which is especially important with simulated data, and verify that predictions are made on the basis of physically plausible features. This ultimately improves the ease of adoption of machine learning techniques. The most used methods to explain machine learning model predictions (such as SHAP and other methods that rely on stochastic sample generation) suffer from high computational complexity and struggle to account for interactions between inputs. *PERTURB-c* addresses these issues by leveraging physical knowledge of the known spectral correlation. For visualisation of this analysis, we propose a heat-map-based representation which is better suited to large numbers of input features along a single dimension, and that is more intuitive to those who are already familiar with retrieval methods. Note that while we chose this exoplanet retrieval context to demonstrate our methodologies, the *PERTURB-c* framework is model agnostic and in a broader context has potential value across a plethora of adjacent regression problems.

**Key words:** Machine Learning – Exoplanets – Atmospheric Characterisation – Data Methods – Interpretability

## 1 INTRODUCTION

Since the first transiting exoplanet observation in 1999 (Charbonneau et al. 1999), the field has blossomed into one of the great scientific frontiers of the 21st century (National Academies of Sciences, Engineering, and Medicine 2018), with over 6000 exoplanet discoveries now having been confirmed<sup>1</sup>, showing remarkable diversity and allowing us to make significant progress in our understanding of planetary formation and evolution. This diversity has shifted attention away from detection and towards characterisation, particularly of the planetary atmospheres (Seager & Deming 2010; Cowan et al. 2015).

Characterising exoplanet atmospheres can answer important questions about planetary formation and evolution, alongside the potential to uncover habitability or presence of potential biosignatures which may even indicate signs of extraterrestrial life (Seager & Deming 2010).

Traditionally within the field, this characterisation of chemical composition and other parameters is performed by iterative physics-based retrievals (Barstow et al. 2020). Given the complex nature of the models to be optimised, these methods can be very computa-

ally intensive. With the advent of machine learning in the field, we can achieve significant acceleration of atmospheric characterisation (Márquez-Neila et al. 2018; Zingales & Waldmann 2018; Cobb et al. 2019; Fisher et al. 2020; Nixon & Madhusudhan 2020; Martinez et al. 2022; Yip et al. 2023; Lueber et al. 2025; Tahseen et al. 2025).

However, we do not see the proliferation of these techniques across the field; while in part this is simply due to the established nature of existing practices, the issue lies also with two other main shortcomings of machine learning based approaches. The first of which being the availability of data: machine learning model accuracy is largely dependent on with the amount of data used for training (Figueroa et al. 2012), and we currently do not have sufficient data (Bashi et al. 2018) to train these tools using real observations. While machine learning tools can be trained using simulated data to predict on real data (Lueber et al. 2025), doing so without imprinting the inherent bias from your data generation and sampling into the trained network is impossible. Determining to what extent bias has been successfully mitigated, and how reasonable and physical predictions are likely to be is then a high priority. This brings us to the second shortcoming of machine learning techniques: their complex nature renders them ‘black-boxes’, whereby obtaining an understandable explanation for the predictions of which is increasingly challenging (Molnar 2018). It is this crucial frontier in which the work done with machine learn-

\* E-mail: j.d.clarke@ucl.ac.uk

<sup>1</sup> <https://exoplanetarchive.ipac.caltech.edu>

ing often falls short not only in this field (Márquez-Neila et al. 2018) but across many others (Weber et al. 2024).

Given that more simplistic models can be easier to interpret than complex ones, there is said to be a trade-off between accuracy and interpretability (Lundberg & Lee 2017). Better understanding of how complex neural networks, such as the ones that are adept at solving the atmospheric retrieval problem, reach their predictions can allow us to inspect for biases in both data and in the model, which is especially important given the simulated nature of the data. It is crucial to help to verify that the model is actually making predictions on the basis of known physically plausible features, or conversely, in the unlikely case, uncover unexpected relationships which may lead to new domain knowledge. Being able to trace model decisions back to physical features<sup>2</sup> in the data is key to there being any lasting scientific value behind the method, and can ultimately help improve the usefulness, reliability and ease of adoption of machine learning techniques.

The common machine learning approach to interpretability is to obscure, permute or perturb aspects of the observation in order to determine the relevance of these features to the prediction (known as *feature importance*) (Molnar 2018). However, in problems in which the observations themselves are highly correlated, by naïvely modifying individual wavelength bin values in an observation it is very easy to arrive at a spectrum which is highly non-physical and therefore not within the learned parameter space of the model (Mase et al. 2020; Ng et al. 2025). Atmospheric retrieval represents one such example of these correlated problems, as there are very specific ways in which each wavelength bin in an observation is subsequently related to the others. At small scales this is due to the effects of spectral line broadening (Guest et al. 2024), which remains an ongoing area of development for our understanding of spectral observations (Buldyrev et al. 2025). At less granular scales, this is due to the overall complex structure of molecular transmission as governed by quantum transitions. As a result of the combination of these both the efficiency and the effectiveness of out-of-the-box feature importance methods at interpreting machine learning retrieval models is poor (Huang & Marques-Silva 2023). Despite this, methods such as *SHAP* (Lundberg & Lee 2017) continue to see popularity, in part due to their ease of implementation. We set out to detail the shortcomings of two main techniques, *ceteris paribus* and also *SHAP* in this application, and in lieu of this propose *PERTURB-c*<sup>3</sup>, a new interpretability framework specifically tailored for highly correlated spectral data.

*PERTURB-c* is designed to mitigate the issues with out-of-the-box feature importance methods when used for interpreting machine learning based retrievals, handling highly correlated spectral data by generating modified spectra which are instead governed by physically motivated relations. This makes the method much more stable in

<sup>2</sup> Here it is necessary to disambiguate between conflicting terminology from machine learning and exoplanetary science: when we just refer to *features* we are referring to the input features of the model, i.e. the individual wavelength bins that are measured. When we refer to *spectral features*, we are referring to regions of spectra which are indicative of certain physical effects, as in “between 4 and 5  $\mu\text{m}$  there is a distinct phosphene *spectral feature*”, where the *spectral feature* in here refers to a collection of adjacent input *features*, or wavelength bins, which are indicative of the presence of phosphene. For clarity, to the degree that this is possible we will try to refer to input features as such, or as wavelength bins, but for established terminology such as ‘*feature importance*’ (which refers to input features) it is necessary to follow machine learning convention.

<sup>3</sup> Perturbation Explainability for Regression Techniques to Understand Retrieval Black-boxes.

situations where out-of-the-box methods such as *SHAP* fail. Using an example model from (Clarke et al. 2026, in prep.), we demonstrate *PERTURB-c* on a simulated case study based on WASP-107b in order to showcase its ability to interpret these types of predictions.

## 2 BACKGROUND

We assume the reader has familiarity with transit spectroscopy methods, however for those from a machine learning background, we include a short overview in [Appendix A](#).

### 2.1 Inference from Exoplanet Observations

For the purpose of dispelling any preconception (which we acknowledge is disproportionately widespread, and largely based in an appeal to tradition) that the reader may have regarding the provenance behind machine learning techniques, first we will detail the current state of non-machine learning techniques for atmospheric retrievals. We do this not to present machine learning techniques as a comprehensive replacement for traditional retrievals but simply to motivate additional diversification of our methodological toolbox, specifically with low-latency strategies for the big data era.

There are currently many options available for sampling algorithms, from those that use MCMC (Foreman-Mackey et al. 2013), those that use nested sampling (Speagle 2020; Feroz et al. 2009) and other more naive sampling methods such as grid sampling. The choice of sampler can have a large effect on the inferred posterior distributions in a retrieval, particularly in the event of strong degeneracies, where there are multimodal likelihood surfaces (Fisher & Heng 2022). Compounding this, there is an increasing menagerie of separate retrieval implementations themselves (MacDonald & Batalha 2023) for the community to choose from which offer an array of different, sometimes even conflicting, solutions for the same data<sup>4</sup> (see Barstow et al. 2020, for a summary). This is before we even introduce the effects of conflicting observations or instrumentation<sup>5</sup> (as discussed in further detail by Welbanks et al. 2023).

This resulting contradiction proliferates a landscape in which authors are compelled to report the results of a number of separate retrieval methods in order to validate the conclusions of their study (see Lustig-Yaeger et al. 2023; Dyrek et al. 2024, as examples of this). The iterative nature of retrieval methods already makes for a very computationally demanding analysis, limiting their use as datasets expand, and the emergence of multi-method validation only stands to compound this problem.

Despite this harsh critique, until very recently these methods remained our only tool for handling observational data of this nature. This means that even with the slow speed and poor scaling issues of traditional retrievals, they are still the most reliable tool for these types of analysis and as such they persist, especially in small sample size studies where scaling imposes much less of a constraint.

### 2.2 Machine Learning Retrievals

The supplementation of traditional Bayesian retrievals with machine learning in order to minimise the computational cost can help us to

<sup>4</sup> See Barstow et al. 2016; Pinhas et al. 2019 for two separate interpretations of the same set of hot Jupiter data from Sing et al. 2016.

<sup>5</sup> See Espinoza et al. 2019 for analysis of ground based observations, in contradiction to Sedaghati et al. 2017’s analysis of space-based observations of WASP-19b.

prepare for the inevitable latency issue which is forthcoming given the rate of increase in data acquisition (Martinez et al. 2022; Yip et al. 2022).

There are two applications for machine learning in this context: surrogate modelling, replacing the computationally intensive atmospheric models, either in part or in full with a pre-trained component (Tahseen et al. 2024), or, solving the inverse problem, replacing the Bayesian minimisation entirely with a learned representation of the parameter space in order to amortise<sup>6</sup> the problem, offloading the simulation of new spectra into a precomputed training dataset of example spectra. This paper will focus on interpreting the latter of these two approaches, solving the forward problem, as it can more robustly describe any number of simulation environments and can also be more of a black-box than surrogacy. Note however that the PERTURB-c methodology can be utilised across a plethora of adjacent regression problems.

By using these machine learning approaches to solve the inverse problem directly (infer chemical abundance directly from reduced spectra) and offsetting the computational expense of inference into a one-time training expense, the trained pipeline can be made comparatively lightweight. Existing work has proven the effectiveness of such techniques in this field, such as Martinez et al. (2022), Yip et al. (2023) and Lueber et al. (2025) (for a full list see MacDonald & Batalha 2023).

### 2.3 Interpretability

Any complex machine learning methodology does however introduce the black box component into the pipeline, wherein it becomes challenging to disentangle the predicted abundances from spectral features in the observed data. The most important aspect that we want to untangle is the feature importance, which is the relative impact of each input wavelength bin in our observed data to the results of our retrieval. This allows for statements to be made such as “we detect phosphine at a  $3\sigma$  confidence level *given that* the uncertainty on the 0.41 micron wavelength bin is within 1%  $R_p/R_s$ ”, which is very important for realistic classification of low confidence detections of molecules with very narrow wavelength signatures, where the whole retrieval may hinge on very few input features.

This feature importance can be achieved with traditional retrievals (Welbanks et al. 2023) through the means of leave-one-out Bayesian methods. Feature importance has also been explored when using their machine learning counterpart (Yip et al. 2021) by modification of select wavelengths sequentially. The ‘modify one’ methodology therefore presents us with a logical starting point for our exploration into improved interpretability. First we should understand the way such techniques work, and their limitations. In order to do this, we present a case study based on simulations of the planet WASP-107b.

## 3 ML RETRIEVAL METHODS IN THIS PAPER

While the showcase in this paper is the methods of interpretability and not the models themselves, for completeness the model frameworks will also be detailed here. The model that we will use for our case study is the dense neural network from Clarke et al. (2026), which is a simple neural network architecture with 3 hidden layers (with layer sizes [103, 128, 256, 128, 8] respectively) which takes as normalised

<sup>6</sup> Amortisation: *The front-loading of an ongoing operating cost into a high one-time initial cost.*

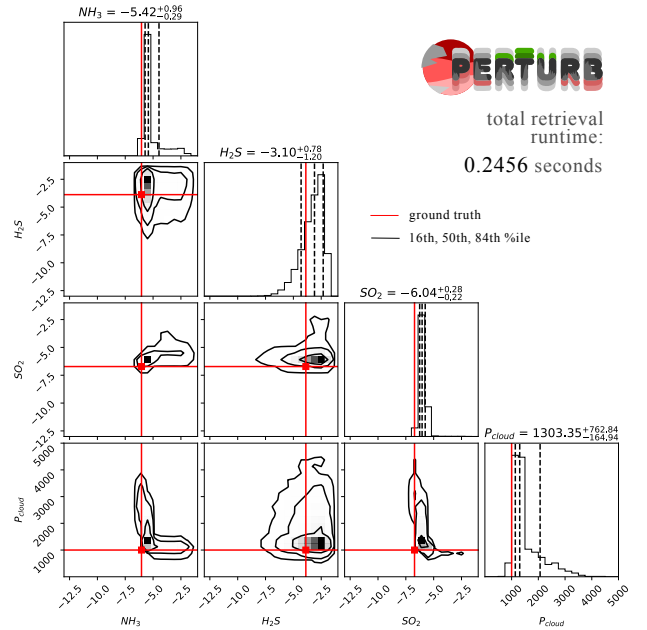


**Figure 1.** Subset of key molecular abundances retrieved by neural network (Clarke et al. 2026) on simulated WASP-107b-like planet for an idealised 100-bin spectrograph. Full retrieval (excluding plotting of corner plot) was performed in 0.2456 seconds using our machine learning accelerated hybrid retrieval strategy, and full corner plot can be seen in Appendix F1.

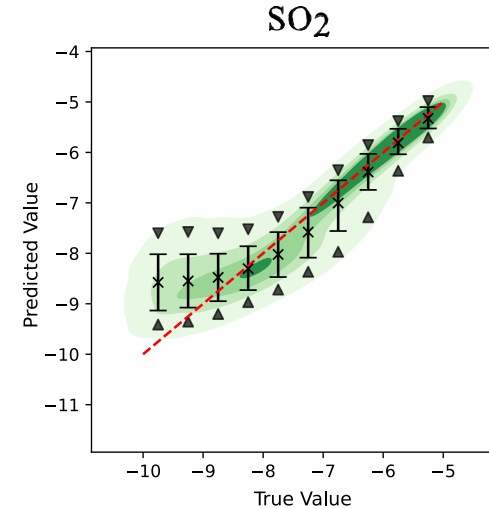


**Figure 2.** The predictive performance of the neural network retrieval for  $SO_2$ . The red dashed line indicates perfect accuracy. Values on both axes are shown in log abundance of  $SO_2$ .

input features the 100 spectral bins, and a randomly sampled estimate of  $H_2O$ ,  $CO_2$ , and  $CH_4$  from the priors. The network estimates as a regression the normalised abundance of the 7 target molecules, and the cloud pressure. A leaky ReLU activation function is utilised for the hidden layers in order to constrain dying neurons within fully connected layers.

The network is retrained using 50,000 simulated planetary observations of super-earth/sub-neptune objects. Uncertainty within the prediction is estimated by use of an ensemble of similar models and the stochastic nature of prior selection, and is fine tuned against

model prediction accuracy on a separate testing dataset. The system characteristics of the planets in these datasets are drawn from Yip et al. (2022) such that the population trends over the dataset are reflective of our current understanding of planet population. The spectra are simulated using TauREx-III (Al-Refaie et al. 2021) with an atmospheric composition comprised from  $H$ ,  $He$ ,  $H_2O$ ,  $CO_2$ ,  $CH_4$ ,  $NH_3$ ,  $H_2S$ ,  $PH_3$ ,  $SO_2$ ,  $SiO$ ,  $TiO$ , and  $VO$ , the abundance of which was drawn randomly from a uniform distribution. Linelists for the aforementioned molecules are from the ExoMol Atlas (Polyansky et al. 2018; Azzam et al. 2016; Bowesman et al. 2024; Chubb et al. 2021; Coles et al. 2019; McKemmish et al. 2019; Sousa-Silva et al. 2015; Underwood et al. 2016; Yurchenko et al. 2022, 2024, 2026). The ranges of the distributions for each molecule can be found in the appendix in tabular form in Table E1 and all parameter distributions visually represented in Figure E2. The atmosphere is assumed to be isothermal, with temperature set at the planet's equilibrium temperature. The atmosphere is vertically discretised into 70 pressure layers from  $10^{-5}$  Pa down to  $10^5$  Pa using an inverse logarithmic grid, and volume mixing ratio is kept constant with altitude. The background atmosphere is comprised of  $H_2$  and  $He$ , with fixed ratio  $H_2/He = 0.1756$ , and the trace species are added with uniform vertical mixing ratio. For simplicity, the host star is assumed to be a blackbody and we neglect to include equilibrium chemistry or photochemistry, and as such abundances are simply defined as free parameters not correlated with pressure or temperature. A uniform grey cloud deck is included, parametrised by a maximum pressure level below which the atmosphere becomes optically thick.

The high resolution output from this modelling is then reduced in accordance with a low resolution hypothetical instrument that has a constant resolution of 26.7, with 100 wavelength bins logarithmically spaced between  $0.4\mu\text{m}$  and  $16\mu\text{m}$ . This relatively wide binning grid was chosen to increase the number of correlated spectral bins and is modelled as an extended AIRS instrument (Mugnai et al. 2021). This represents a ‘worst case’ scenario as it encompasses both the low wavelength  $TiO$  and  $VO$  dominated regime and also the higher wavelength  $SO_2$  and  $PH_3$  spectral features, as well as large regions of the more broad  $H_2O$  and  $CH_4$  spectral features. This is to say that any observation from this hypothetical instrument has a complex correlation structure that will contain both pairs of wavelength bins in which there is large amounts of correlation, and also pairs of wavelength bins that can be almost completely uncorrelated, making it very challenging for any interpretability method to accurately produce realistic samples.

This simplified set of assumptions allows for the generation of large and diverse quantities of training data for the network, while remaining an appropriate substitute for the real problem. The performance of the network across the test set, a sample of planets drawn from the remaining samples in Yip et al. (2022) which is representative of, but crucially not subset to, the training set, is visualised in Figure 2.

#### 4 WASP-107b AS A CASE STUDY

To demonstrate the retrieval and interpretability framework, a simulation was drawn from the test dataset to resemble recent observations of WASP-107b, specifically the petitRADTRANS retrievals done by Dyrek et al. (2024). Despite the existence of real JWST observations of WASP-107b simulated data gains us several advantages over real data in the context of evaluating the methodology. By using simulated data rather than a real observation we can focus on the performance of the techniques without concern for interference from external fac-

Parameter	Unit	Value
H2O	log abundance	-3.81
CO2	log abundance	-8.49
CH4	log abundance	-8.83
NH3	log abundance	-6.04
H2S	log abundance	-3.88
PH3	log abundance	-7.60
SO2	log abundance	-6.72
SiO	log abundance	-9.03
TiO	log abundance	-11
VO	log abundance	-11
Cloud Pressure	Pa	1,000
Planet Mass	Earth Masses	30.5
Planet Radius	Earth Radii	10
Planet Temperature	K	770
Stellar Radius	Solar Radii	0.67
Stellar Temperature	K	4,425

**Table 1.** This table shows the ground truth atmospheric abundances, alongside system bulk properties and temperatures, used in the generation of the WASP-107b case study.

tors such as stellar variability (Thompson et al. 2023) or instrument noise (Rustamkulov et al. 2022, JWST specific) which can have a strong impact on the data, allowing for a more objective assessment of the framework in absence of other influence. Most importantly however it allows us to draw comparisons with a ground truth value, which we otherwise would not have.

The simulated observation contains a significant proportion of  $SO_2$  in the planetary atmosphere which can be constrained by the trained network. As seen in Figure 1, we can assess the performance of the model as good, as the ground truth molecular abundance falls within the posterior distribution (the potential set of molecular abundances predicted by the machine learning model). That being said, the focus of this work is not the performance itself, but rather obtaining reliable explanations of the model’s predictions.

The high resolution data is calculated using the TauREx III (Al-Refaie et al. 2021) forward model, with line lists from the ExoMol Atlas (Tennyson & Yurchenko 2018) in keeping with the data generation for the training set. We used a uniform grey cloud model with a cloud pressure of 1000 Pa. This high resolution output is then reduced in line with the training dataset to resemble an observation from the low resolution hypothetical instrument.

#### 5 FORMALISING THE MACHINE LEARNING RETRIEVAL PROBLEM

The machine learning model, which we shall denote as a function  $f$ , is trained on a set  $\mathbf{X}$  of  $N$  training datapoints (observations) which are pairs of the form  $(\mathbf{x}_n, \mathbf{y}_n)$ ,  $\forall n \in [1, \dots, N]$ , where  $\mathbf{x}_n = [x_1, x_2, \dots, x_M] \in \mathbb{R}^{1 \times M}$  corresponds to a spectrum consisting of  $M$  wavelength bins  $x_{n,m} \in \mathbb{R}$ ,  $\forall m \in [1, \dots, M]$  and  $\mathbf{y}_n = [\log(NH_3), \log(H_2S), \log(SO_2), \dots] \in \mathbb{R}^{1 \times P}$  is a vector representing the  $P$  atmospheric parameters (here molecular abundance of each atmospheric gas) to be predicted. We shall denote the *unknown* distribution from which  $\mathbf{x}_n$  is sampled as  $\mathcal{D}$ . Given an observed spectrum  $\mathbf{x}_\star$  as input, the model can output the predicted atmospheric parameters as  $\hat{\mathbf{y}}_\star = f(\mathbf{x}_\star)$ . Note that the forward model that generated the data can be viewed as a function  $g$  that generates a spectrum using as inputs the ground truth atmospheric abundances,  $\mathbf{x}_\star = g(\mathbf{y}_\star)$ . In other words, the machine learning model  $f$  serves as

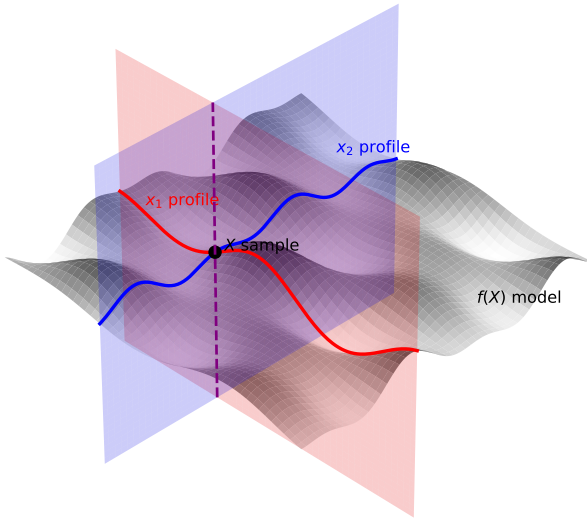


**Figure 3.** Ceteris paribus profile visualisation for the simplest 2D case. For a model  $\hat{y} = f(\mathbf{x})$  with input features (or wavelengths)  $x_1$  and  $x_2$ , which predicts the abundance of one molecular species  $y$ , the ceteris paribus profiles for both input features of a specific given observation  $\mathbf{x}_n$  are visualised.

an approximation of the inverse of the forward model  $g$ , i.e.  $f \approx g^{-1}$ . For the rest of the paper, we shall drop the index  $n$  when it is clear that we refer to a specific sample for readability.

## 6 CETERIS PARIBUS PROFILES

*Ceteris paribus*<sup>7</sup> profiles are one of the simplest forms of explanation for black box functions. They are used to characterise how the model responds to variations in input values. The premise of ceteris paribus represents the simplest experiment you can perform to characterise a system: vary one input feature while keeping all others constant, and measure the resulting change in the output (in our case, the output is the molecular abundance of a single species). Despite this naïve approach, ceteris paribus profiles allow for a visualisation of the complex curvature of the model function's surface, projected into the dimension representing a single input feature for all other input features being fixed at a set value (Biecek & Burzykowski 2021). This can provide a very powerful description of the local parameter space around the fixed features. For a one dimensional problem, this can be a complete global picture of the system. For a two dimensional system as in Figure 3, this is a good approximation of the immediate parameter space surrounding the observation. As dimensionality increases, however, the parameter space becomes orders of magnitude more complex, so that at high dimensions, this method is substantially less informative.

To use the ceteris paribus method for local explainability (i.e. to explain the model's prediction on a single datapoint), fix all input wavelength magnitudes to the values in the observation, and in turn modify these magnitudes to build up slices of the complex curvature of the model function's surface, which all intersect at the point represented by the true observation as shown in the 2D case in Figure 3.

This can be described more formally, such that for a given observation  $\mathbf{x}_\star$ , we can calculate the response of the model to change in the value  $x_{\star m}$  of wavelength bin  $m$  by retrieving abundances over a set

of modified observations. To generate the modified observations, we first must ascertain a reasonable range over which the model could expect change. In this case we can look to the maximum and minimum for the column vector of the full training data  $\mathbf{X}$  at wavelength  $m$ , i.e the max & min values of  $\mathbf{x}_m$  across all  $N$  training datapoints,

$$x_m^{\min} = \min_n x_{n,m}, \quad x_m^{\max} = \max_n x_{n,m}. \quad (1)$$

Using this context, a linear grid of  $K$  values between these,  $\mathbf{z}_m \in \mathbb{R}^{1 \times K}$ , can be constructed:

$$z_{m,k} = x_m^{\min} + \frac{(k-1)(x_m^{\max} - x_m^{\min})}{K-1}, \quad \forall k \in [1, 2, 3, \dots, K]. \quad (2)$$

As such we can define, where the operator ' $\coloneqq$ ' denotes value assignment, our set of modified observations  $\mathbf{X}'_m \in \mathbb{R}^{K \times M}$  where the  $m^{\text{th}}$  wavelength bin is replaced with each of the intensity values from  $\mathbf{z}_m$  in turn,

$$\mathbf{x}'_{m,k} = \mathbf{x}_\star |_{x_{\star m} \coloneqq z_{m,k}}, \quad \forall z_{m,k} \in \mathbf{z}_m, \quad (3)$$

and *all other values being equal*, i.e. left the same as in the initial observation  $\mathbf{x}_\star$ . This set of modified observations are then specific to the observation  $\mathbf{x}_\star$ . By subsequently retrieving abundances for all modified observations we can discretely characterise the modified retrieved abundances  $\hat{\mathbf{Y}}'_m$  (Molnar 2018) as

$$\hat{\mathbf{Y}}'_m = f(\mathbf{X}'_m). \quad (4)$$

The response profile  $\mathbf{r}_m \in \mathbb{R}^{K \times 1}$  for the specific wavelength bin  $m$  is such that it maps the relative effect of deviation  $\mathbf{z}_m - x_{\star m}$  onto the relative deviation in retrieved abundance of a specific molecule, say  $\hat{y}'_{m,SO_2} \in \mathbb{R}^{K \times 1}$ , i.e.

$$\mathbf{z}_m - x_{\star m} \odot \mathbf{r}_m = \frac{\hat{y}'_{m,SO_2} - \hat{y}_{\star SO_2}}{\hat{y}_{\star SO_2}}. \quad (5)$$

The main advantages to ceteris paribus are that it is typically fast, model agnostic, and can work well if feature contributions are independent. The main drawback to ceteris paribus profiles is that in the case of non-independent input feature interactions, some, if not most of the set of modified observations generated by the method can be non-physical. These out of distribution samples prompt unstable model response, which is not useful to learn.

For example, even if the range of the  $0.41 \mu\text{m}$  wavelength bin extends up to 5%  $R_p/R_s$ , this can only be the case for very PH3-saturated atmospheres, in which case the  $0.38 \mu\text{m}$  and  $0.45 \mu\text{m}$  wavelength bins would also be high. If our given observation  $\mathbf{x}_\star$  is a phosphene depleted atmosphere, naturally the  $0.38 \mu\text{m}$  and  $0.45 \mu\text{m}$  wavelength bins will be low, so the majority of  $\mathbf{X}'_m$  modified observations (with high  $z_k$ ) will be non-physical, in other words,

$$\mathbf{x}'_{m,k} \not\sim \mathcal{D}, \quad \forall z_{m,k} \in \mathbf{z}_m. \quad (6)$$

There are modifications to how the values of  $z_{m,k}$  are determined that can be made to help mitigate this, such as those in SHAP.

## 7 SHAPLEY ADDITIVE VALUES

Shapley values are a concept from coalitional game theory, used to quantify the individual (marginal) contribution of each player to a team's 'outcome' in a team game. They determine each player's contribution by considering how much the overall outcome changes when they join each possible combination of other players, and then

<sup>7</sup> Latin: "other things (being) equal".

	$\mathbf{X}'$			$\mathbf{X}''$			
$\mathbf{x}'_1$	$x_{\star 1}$	$x_{\star 2}$	$x_{\star 3}$	$\mathbf{x}''_1$	$\bar{x}_1$	$x_{\star 2}$	$x_{\star 3}$
$\mathbf{x}'_2$	$x_{\star 1}$	$x_{\star 2}$	$\bar{x}_3$	$\mathbf{x}''_2$	$\bar{x}_1$	$x_{\star 2}$	$\bar{x}_3$
$\mathbf{x}'_3$	$x_{\star 1}$	$\bar{x}_2$	$x_{\star 3}$	$\mathbf{x}''_3$	$\bar{x}_1$	$\bar{x}_2$	$x_{\star 3}$
$\mathbf{x}'_4$	$x_{\star 1}$	$\bar{x}_2$	$\bar{x}_3$	$\mathbf{x}''_4$	$\bar{x}_1$	$\bar{x}_2$	$\bar{x}_3$

**Figure 4.** Visualisation of the set of possible coalitions relevant for determining the relative contribution of wavelength  $x_{\star 1}$  for a simplified observation with only  $M = 3$  wavelength bins. The coalitions are split into those including wavelength  $x_{\star 1}$  and those excluding it ( $\mathbf{X}'$  and  $\mathbf{X}''$ , respectively).

averaging those changes. In essence, it calculates each player's average marginal contribution across all possible *coalitions* (subsets of players included in the team). The concept has found application in the context of determining the individual contribution of each feature to a machine learning model's output (Lundberg & Lee 2017). In this setting, each input feature (here: wavelength) corresponds to 'a player', and 'the outcome' to the model's output (here: retrieved abundance). The Shapley values can then capture the contributions of each wavelength to the predicted abundance relative to the average sample.

For a given feature  $x_m$ , the SHAP value  $\phi_m$  is defined as the average marginal contribution of that feature across all possible subsets of the other features, i.e.

$$\phi_m = \sum_{S \subseteq M \setminus \{x_m\}} \frac{|S|! (|M| - |S| - 1)!}{|M|!} [f(S \cup \{x_m\}) - f(S)],$$

where  $M$  is the set of all features,  $S$  is a subset of features not containing  $x_m$  and  $f(S)$  denotes the model output when only features in  $S$  are present. The weighting term ensures equal consideration of all feature orderings.

In other words,  $\phi_i$  represents the expected change in the model prediction when feature  $x_i$  is added to a randomly chosen subset of the remaining features. Due to its inherent combinatorial nature the complexity of the method explodes exponentially with the number of input features (given  $M$  features, there are  $2^M$  possible coalitions to consider).

Shapley values can be calculated by comparing pairs, of ceteris paribus values rather than calculating full profiles. We will demonstrate this using a simplified observation with only  $M = 3$  wavelength bins,

$$\mathbf{x}_{\star} = [x_1, x_2, x_3] \quad (7)$$

and the same dataset of physically possible observations  $\mathbf{X}$ . The Shapley value of the first wavelength bin,  $m = 1$  is calculated by taking the difference in ceteris paribus values for all possible coalitions of  $\mathbf{x}_{\star}$  and the expected observation  $\bar{\mathbf{x}}$  [Figure 4],

$$\mathbf{X}'_m = \left[ \begin{array}{c} \mathbf{x}_{\star} \\ \mathbf{x}_{\star} \Big|_{x_{\star 2} := \bar{x}_2} \\ \mathbf{x}_{\star} \Big|_{x_{\star 3} := \bar{x}_3} \\ \bar{\mathbf{x}} \Big|_{\bar{x}_1 := x_{\star 1}} \end{array} \right]. \quad (8)$$

For each of these coalitions which contain the target value is a respective coalition,  $\mathbf{X}''_m$ , without it<sup>8</sup>,

$$\mathbf{X}''_m = \mathbf{X}'_m \Big|_{x'_{m,1} := \bar{x}_1 \mathbf{1}_K}, \quad (9)$$

where  $K = \frac{2^M}{2}$ , half the total number of possible coalitions or the number of which retaining the target sample value in the target wavelength bin.

By defining the difference in response  $\Delta \hat{\mathbf{Y}}'_m$  between all corresponding pairs of coalitions

$$\Delta \hat{\mathbf{Y}}'_m = f(\mathbf{X}'_m) - f(\mathbf{X}''_m), \quad (10)$$

the Shapley value,  $\phi_m$ , is then given by the expectation value of this difference,

$$\phi_m = \mathbb{E}(\Delta \hat{\mathbf{Y}}'). \quad (11)$$

As such to calculate Shapley values for all wavelength bins in an observation, model inference scales by  $O(2^M \times M)$ . For an observation with 100 wavelength bins, this is  $2.5 \times 10^{30}$  iterations.

As can be seen, calculating true Shapley values is not feasible for most use cases, as is also true here with retrievals. In the most widespread implementation of Shapley value explanation, SHAP (Lundberg & Lee 2017), the monte carlo approximation (Štrumbelj & Kononenko 2014) is used, wherein a random number of feature values are replaced from the random drawn sample, not an exhaustive set of possible coalitions. This subset of coalitions  $\tilde{\mathbf{X}}'_m$  is optimised such that it captures as much of the information content of  $\mathbf{X}'_m$  as possible, minimising divergence  $D$  for the informative samples. In other words,  $D(\tilde{\mathbf{X}}'_m | \mathbf{X}'_m) \rightarrow 0$ . Uninformative samples are then selected correspondingly, not optimised.

By reducing the number of samples  $K$  which are drawn, the model inference required can be reduced so that it scales by  $O(2M \times K)$ .

Similarly as above with ceteris paribus profiles, it stands that any given modified sample could be out of distribution with the prior training data such that

$$\tilde{\mathbf{x}}'_{m,k} \not\sim \mathcal{D} \text{ nor } \tilde{\mathbf{x}}''_{m,k} \not\sim \mathcal{D}, \quad \forall k \in [1, \dots, K]. \quad (12)$$

But more globally SHAP suffers from the fundamental logical flaw in that, given data has some correlation, the mean *uninformative* sample is not necessarily in the underlying distribution given by the prior training data. For comparison of correlation, we will use the Pearson rho metric between two wavelengths  $\rho(x_a, x_b)$  like so, which gives us values between  $-1$  (negatively correlated) and  $1$  (positively correlated), with  $0$  being no correlation. Using this, we can express

$$\bar{\mathbf{x}} \not\sim \mathcal{D}, \quad \forall \mathbf{X},$$

$$\text{given that } \sum_{m'} \left[ \rho(\mathbf{x}_{:,m} \mathbf{1}_{(M-1)}^T, \mathbf{X}_{:,m \setminus m'})^2 \right] \gg 0, \quad (13)$$

$$\forall m \in [1, \dots, M].$$

Given the latter is true, it must then follow that former is also true, as  $\mathbf{x}'_k = \bar{\mathbf{x}}$  for some value of  $k$ .

In data regimes where the points are highly correlated like spectral retrieval, ceteris paribus style methods suffer heavily from the generation of out-of-distribution samples. While this effect is mitigated to a certain extent by the SHAP package's utilisation of prior sampling, mixing features from two spectra randomly or exhaustively almost never produces a coherent modified observation. Where SHAP excels in comparison to pure ceteris paribus is that by taking a difference as

<sup>8</sup> Here we use the one vector of size  $N$  such that  $\mathbf{1}_N = (1, 1, \dots, 1) \in \mathbb{R}^{N \times 1}$  to describe the transform  $x'_{m,m',1} := \bar{x}_1, \forall m' \in [1, \dots, \frac{2^M}{2}]$ .

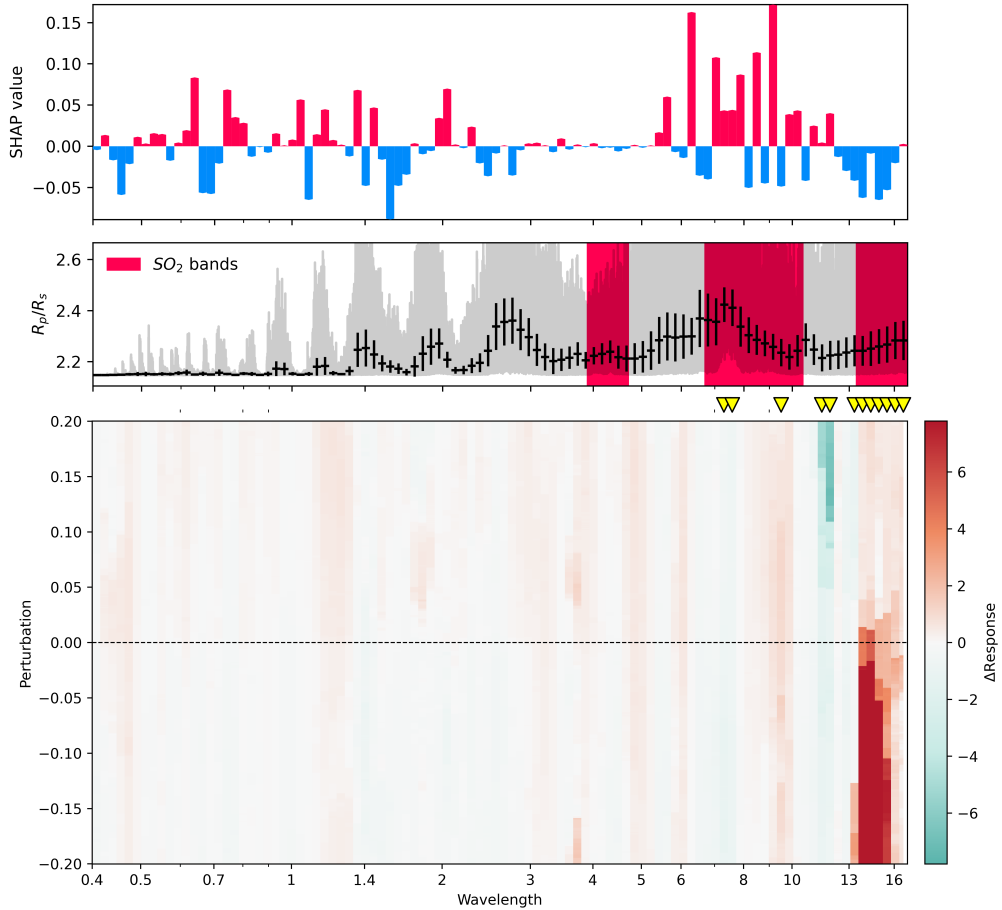


**Figure 5. (Top)** SHAP interpretability for the prediction of  $SO_2$  in WASP-107b case study sample, shown as positive (red) and negative (blue) feature importance bars. **(Middle)** SHAP is accurately assigning importance to the upper end of the observation, but beyond that, there is very little correlation between the SHAP interpretability and the observation datapoints (black) or the  $SO_2$  contribution bands (red). The wavelength regions where  $SO_2$  is the dominant molecule ought to correlate with positive feature importance given that the model has accurately captured the feature representation, but due to the effects of correlation, this has not been captured by the SHAP analysis. **(Bottom)** The PERTURB-c analysis however clearly highlights that the model is focusing on defining the leading edge of the  $SO_2$  band at around  $13\mu\text{m}$ . The high abundance prediction is given due to the combination of transmission in this band being high, and the presence of the band gap at  $12\mu\text{m}$  (more on how to read PERTURB-c plots in Figure 12).

opposed to a raw value, it can nullify these extreme nonsense values. However, a large portion of SHAP’s characterisation still explores physically impossible regions of the parameter space, which raises concerns over the efficiency of the method for these highly correlated use-cases.

Work has been carried out into how to mitigate this (Mase et al. 2020) and avoid generating out of distribution samples in a problem agnostic way. This approach however is not optimal given that the specific nature of correlation within spectral samples is very well understood, in this field we can likely do better by applying existing domain specific knowledge over inferring it.

Lets apply a standard SHAP interpretation of our model’s prediction for  $SO_2$  abundance in the WASP-107b data [Figure 5]. At a first glance the overall SHAP bar plot is quite overwhelming when visualising this many wavelength bins, but even at closer inspection the peak SHAP values do not seem to align with any regions of interest. While SHAP is capable of identifying the broad region that the model relies on for the detection of phosphine, it is not particularly successful at handling complex reliance on multiple correlated regions. The SHAP values have poor correlation with areas

of expected importance (regions where  $SO_2$  is the dominant contributor), as poor contextualisation of the inter-data correlation results in over-exploration of the out of distribution region.

## 8 PERTURB-c

PERTURB-c aims to reshape interpretability by providing accurate characterisation of the model response at a per-data-point level. Over-simplification of the complex nature of machine learning response is not the route to explainability.

Ceteris paribus profiling is a very effective tool for data we can be certain is uncorrelated; the correlation of features within exoplanet spectra is very well characterised. This means that there exists a problem in which we can interpret some less correlated representation of the spectra using a ceteris paribus technique.

While this is true in isolation, it is important to remember that the whole focus of using these interpretability techniques is increased transparency. There is little value to understanding the model interpretation of some complex reduction of the observed data where there is no clear relation back to the observation. Therefore, a balance

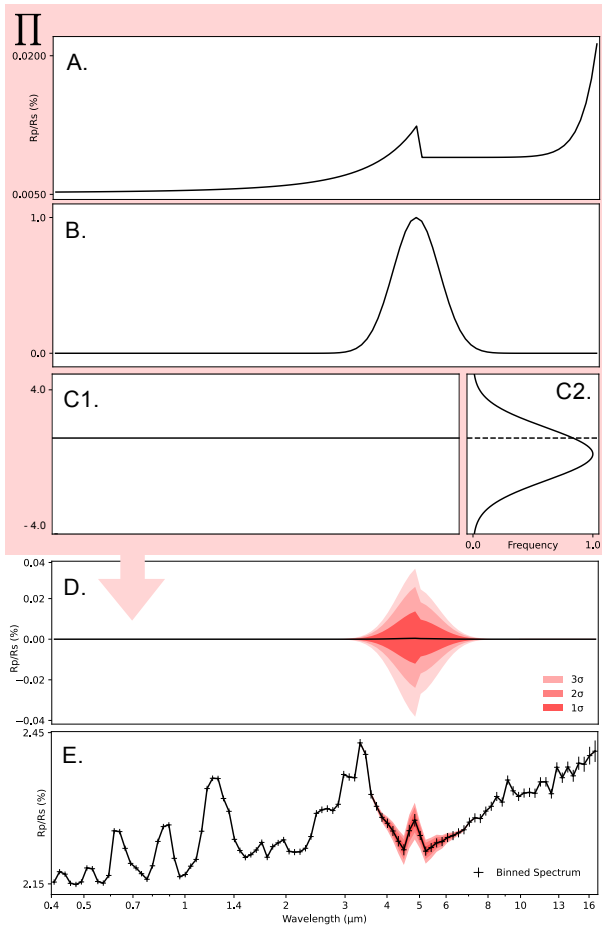


**Figure 6.** Augmented sample generation as performed by PERTURB. Perturbations are calculated as the product of *A*, instrument response, *B*, the perturbation window, which is in this case a Gaussian profile in log wavelength space, and *C1*, the perturbation magnitude coefficient, which is drawn from a standard normal distribution *C2*. A statistical summary of the full perturbation distribution is then shown *D*. The sum of this and the observed data *E* is then the set of modified observations for model analysis. *Note*: the width of the perturbation window has been exaggerated here for visual clarity

needs to be struck where modified observations can be created which lie within the training distribution (are physical) but are not defined by an overly complex or arbitrary function.

As a result of this, rather than remove the correlation from the spectra, it is more logical to impose a set of rules governing the selection of wavelengths which are to be modified such that correlations are maintained. The first order of correlation between any two datapoints in an atmospheric spectrum is wavelength proximity. This means that on average adjacent datapoints will be more correlated than non-adjacent datapoints, and is shown for all combinations of wavelength bins in [Figure 7](#). This is as a result of broad spectrum emission from some of the more abundant molecules. Looking towards more and more exotic atmospheres containing molecules with very narrow spectral signature, this correlation will decrease, but ultimately still dominates at low resolution. As long as adjacent wavelengths remain part of the same coalition, then generated samples should be much more physical.

PERTURB-c approaches the non-physical sample generation problem by probing the response of a cluster of adjacent bins de-

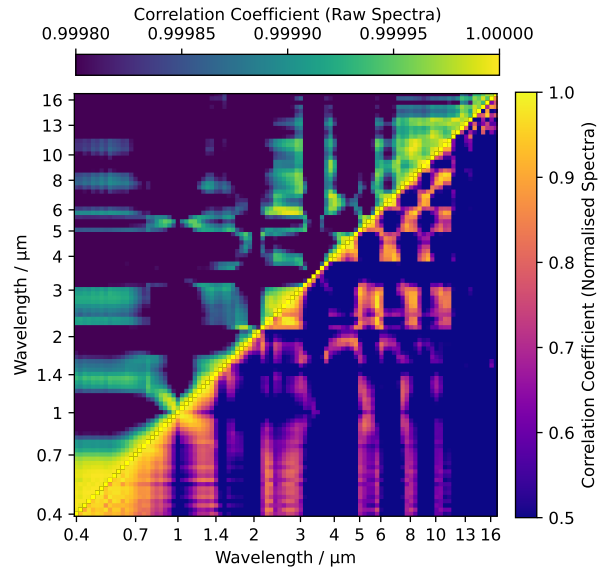


**Figure 7.** Pearson correlation matrix for all wavelength bins across the training dataset. The upper triangular half of the matrix shows the correlation between pairs of wavelength bins in the raw spectra, and the lower triangular half between pairs of wavelength bins in the normalised spectra, as seen by the network. Note that the full correlation matrices would be symmetric about  $x=y$ , so only half of each is shown.

fined by a Gaussian mask [Figure 8](#). This Gaussian assumption holds as an approximation to first order correlation. The optimal width of the Gaussian (defined as constant in the bin scale, not the wavelength scale) is dependent on the target molecule, and is left as a hyperparameter. The use of a wider window will reduce feature importance resolution, however a narrower window will generate more non-physical samples and reduce the power of the technique. Therefore the optimal Gaussian is one that matches the feature scale of the molecule that we aim to capture, and best practice with the technique would involve exploring several scales in tandem before settling on the largest one which is capable of sufficiently capturing the fine scale structure required. It is important to note that this assumption holds better at some wavelengths than at others, so we have to be wary of specific wavelengths which are receiving poor representation under this static Gaussian assumption. It is always recommended to validate the assumption using this type of analysis on some sampling of the parameter space (although it does not necessarily need to be the full training dataset as in this case for brevity).

To remain within physical limits, rather than sampling from unrelated physical priors, the maximum permissible deviation is set using the instrument noise profile for the target observation. The modified observations then form part of a set of possible true observations given the observed data.

Logically it follows that this method of data augmentation produces less spurious samples than the SHAP implementation, but it can also be visualised in a lower dimensional representation for clarity. UMAP analysis<sup>9</sup> of the full dataset [\[Figure 9\]](#) shows a 2 dimensional reduced representation of the spectra which are ‘in-

<sup>9</sup> While we recognize the limitations and potential issues associated with dimensionality reduction techniques, they are employed here solely as a means of providing additional visual clarity. We chose to use UMAP reduction of the data despite the fact that its representation can be influenced by parameter

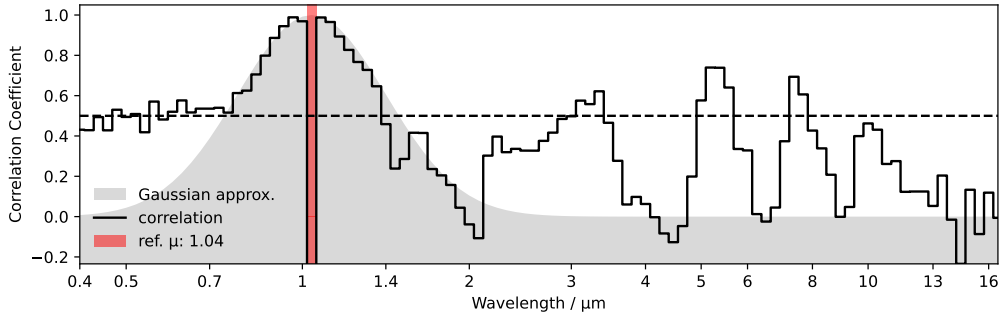


**Figure 8.** Per wavelength Pearson correlation of other datapoints against the  $1.04\mu\text{m}$  wavelength bin (in red) across all training data. See overplotted Gaussian as a close approximation of first order correlation. There are some exceptions to the general trend, in the  $3.5$ ,  $5.5$ , and  $8\mu\text{m}$  regions, but overall to 1st order (dashed line depicts  $>0.5$  pearson correlation) the correlation can be described as a Gaussian centred on the target  $1.04\mu\text{m}$  wavelength bin. Note that while this correlation holds for the majority of reference wavelengths, see [Figure C1](#) for examples of outliers.

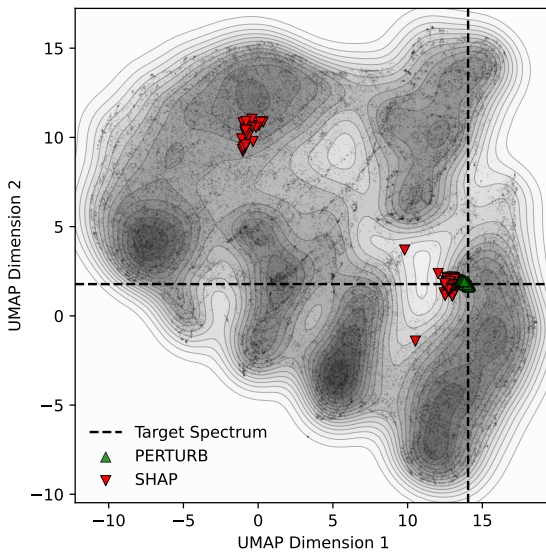


**Figure 9.** UMAP reduced dimensionality representation of the full spectral population represented by the training dataset, the target spectrum is shown by the black dashed lines. The set of modified spectra produced by PERTURB-c are shown in green up arrows, and the set of modified spectra produced by SHAP are shown in red down arrows. Notice the PERTURB-c modified spectra are all clustered around the target spectrum, whereas a non-negligible section of SHAP modified spectra are significantly out of distribution for the target spectrum. This shows the inefficiency of SHAP analysis in high correlation data environments.

distribution' for the model. We can expect the model performance for spectra inside this region to be stable. However, for spectra that appear 'out-of-distribution' (outside of this point cloud), the performance of the model is completely uncharacterised, and, in line with [Ng et al. \(2025\)](#) we hypothesise is unlikely to represent any physical phenomenon.

The case study spectrum in this paper appears in a region of relatively high density, as it is generated in accordance with a physical model and therefore internally consistent with what we would expect from a spectral observation. As the SHAP augmented spectra are generated by combining different data samples, not in accordance

choices and data density, as it is not our intention to provide any quantitative evidence from the embedding itself.

Method	Execution Time / s	Speedup
SHAP ( <a href="#">Lundberg &amp; Lee 2017</a> )	5.3159	$\times 1$
PERTURB-c (T1)	0.0234	$\times 227$
PERTURB-c (T2)	0.2456	$\times 22$

**Table 2.** The execution times for SHAP and the two PERTURB-c tiers (T1 50 samples and T2 2, 000 samples) on analysis of the WASP-107b showcase retrieval. Speedup is calculated relative to the base SHAP method.

with any physical model, they are not necessarily required to be internally consistent in line with the stringent set of correlations that we would expect from a physical spectral observation. It is very likely that the SHAP augmented spectra may exhibit features which are non-physical, which can be represented here as having large separation from the target observation. This is not intrinsically bad when it comes to the accuracy of the method per se, but very little information about the model response in the immediate region surrounding the target observation can be gained when probing the model response non-uniformly at such large separation, and as such data efficiency of the method is poor.

Conversely, as the generation of PERTURB-c augmented spectra is governed by physical limits which maintain expected correlation, the method's coverage of the model response in the immediate region surrounding the target observation is much better. On average in this highly correlated environment only 1 in 200 SHAP samples are in-distribution, whereas PERTURB-c samples are generated such that they should all be in-distribution. As such, PERTURB-c needs to generate a reduced number of samples (approximately  $200\times$  fewer than SHAP) in order to extract the same information content (same number of in-distribution samples) [\[Table 2\]](#). Given the already low inference time of the model in question, this can instead be leveraged to provide additional response resolution (see [Section 11](#)).

## 9 MATHEMATICAL FRAMEWORK & METHODOLOGY

We can formalise this methodology, which is also visualised in [Figure 6](#); first we lay out the known nature of the relationships in our data. As is common in physics notation, we can define a neighbourhood  $\mathcal{N}(\varepsilon, m)$  which is a nonspecific clustering of values that are within some small distance  $\varepsilon$  of a given point  $m$ :

$$\mathcal{N}(\varepsilon, m) = i|_{|i-m| < \varepsilon}; \quad \mathcal{N}(\varepsilon, m) \in \mathbb{R}^{1 \times \ell}. \quad (14)$$

Using this notation allows us to define the relationship where neighbouring points are more positively correlated than non-neighbouring points,

$$0 \approx \frac{1}{M-\ell} \sum_{m=1}^{M-\ell} \left[ \rho \left( \mathbf{x}_{:,m} \mathbf{1}_{(M-\ell)}^\top, \mathbf{X}_{:,m \setminus N(\varepsilon, m)} \right) \right] \quad (15)$$

$$< \frac{1}{\ell} \sum_{m=1}^{\ell} \left[ \rho \left( \mathbf{x}_{:,m} \mathbf{1}_\ell^\top, \mathbf{X}_{:,N(\varepsilon, m)} \right) \right].$$

For example, in [Figure 7](#), we see that there are no cases of strong negative correlation in the data.

Our experiments [\[Figure 8\]](#) can go further to show that the magnitude of correlation between wavelength bins is inversely related to the distance in between the bins. This relationship seems to hold down to a Pearson value of around 0.5, so we can say that

$$\varepsilon \propto -\rho \left( x_m, x_{N(\varepsilon, m)} \right) \text{ to first order.} \quad (16)$$

In practice, we can define this as a windowing function  $w_{\text{gauss.}}(\varepsilon, m)$  with a Gaussian weighting,

$$w_{\text{gauss.}}(\varepsilon, m) = \exp \left( -\frac{16 \ln 2 (\mathbf{m} - \mathbf{m})^2}{\varepsilon^2} \right). \quad (17)$$

With the data correlation constrained in this way, it becomes far easier to generate samples which are consistent with the prior distribution. By applying the windowing function which has been found to approximate the real data correlation, we can ‘diffuse’ the way in which perturbation is applied, allowing for generation of significantly more in distribution samples [\[Figure 9\]](#).

Rather than sampling an even grid of perturbation magnitudes, it is better to apply weighting here also. If we again consider the 2D case, as is far more intuitive to visualise, the diagonal intra-sample distance of each modified  $x_1$  sample to the closest corresponding  $x_2$  sample increases as the square law of the distance from the target sample [Figure 10](#). In higher dimensions, the multidimensional intra-sample distance increases as the power law of the distance from the target. This means that uniform sampling strategies produce sample densities which are inhomogeneous across rotational transformation; the distribution becomes overly concentrated along one dimension while remaining sparse in all others. There are methods to account for this which would result in a totally uniform sampling strategy, however in high dimensionality these produce very sparse sampling at small separation from the target. As such, a tradeoff is reached whereby any method that clusters samples around the target performs more efficiently than linear sampling. We sample from a normal distribution in order to achieve this effect [\[Figure 10\]](#). The added stochasticity helps reduce aliasing bias caused by sinusoidal features or artifacts in the data which may align with any fixed sampling regime.

Given a known instrument noise  $\sigma$ , the random perturbation scale at wavelength  $m$ ,  $\xi_m$  is drawn from a normal distribution with deviation based on the known instrument noise at that wavelength  $\sigma_m$ ,

$$\xi_{m,k} \sim \mathcal{N}_{\text{norm.}}(0, \sigma_m), \quad \forall k \in \mathbf{k}. \quad (18)$$

Combining these two factors the perturbation response is then calculated. For a given observation  $\mathbf{x}_\star$ , the individual response  $\mathbf{r}_m$  of the region centred on wavelength  $m$  can be calculated for all molecules by retrieving the set of abundances as  $\hat{\mathbf{Y}}'_m = f(\mathbf{X}'_m)$  over the subset of modified observations

$$\mathbf{X}'_m = \mathbf{1}_K \mathbf{x}_\star + \xi_m^\top w_{\text{gauss.}}(\varepsilon, m), \quad (19)$$

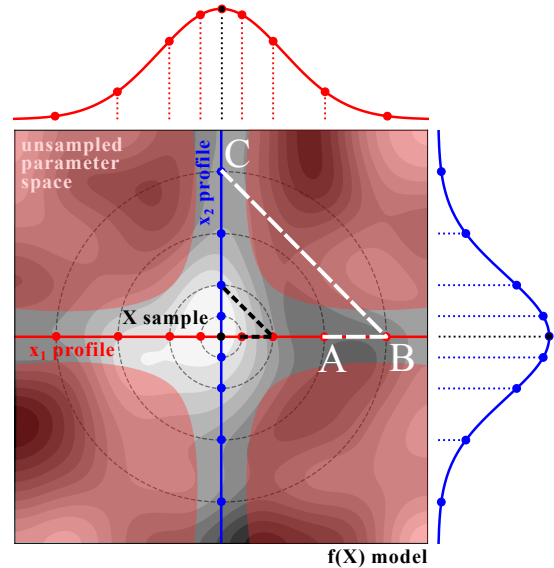


**Figure 10.** As in [Figure 3](#), for a two dimensional problem, we visualise the model  $f(\mathbf{X})$  as a heatmap. The  $x_1$  and  $x_2$  profiles (red and blue respectively) are where we can draw samples. If we were to take samples linearly along each profile, as we take samples which are further from the observation  $\mathbf{x}_\star$  at the centre of the diagram, the ratio of collinear sample density ( $A \leftrightarrow B$ ) to intraprofile sample density ( $B \leftrightarrow C$ ) becomes increasingly large. By instead drawing the applied perturbation scale from a normal distribution, the majority of samples are placed nearer to  $\mathbf{x}_\star$ . This decreases the density of collinear samples at large separation from the observed spectra, which stabilises the exponential nature of the ratio of collinear to intraprofile sample density. This sampling methodology means that sample density is distributed more efficiently, and overall allows us to more comprehensively capture both detail and wider context of the relevant model topology.

and comparing this against the retrieved abundances  $\hat{\mathbf{y}}_\star$  for the zero-perturbation observation where  $\hat{\mathbf{y}}_\star = f(\mathbf{x}_\star)$ , to get the perturbation response

$$\mathbf{R}_m = \mathbf{1}_K \hat{\mathbf{y}}_\star - \hat{\mathbf{Y}}'_m. \quad (20)$$

The neighbourhood or kernel size  $\varepsilon$  can be adjusted as a tunable hyperparameter to control the sensitivity of the method to align with the spectral signature of the target molecules. As previously discussed, it is best practice to explore a range of values for this before settling on one which provides a good balance between both small and large scale features.

## 10 PROSPECTIVE POWER & TIER 1 ANALYSIS

PERTURB-c can be calculated for any arbitrary number of perturbed samples, which translates into different levels of effective resolution into the model response. Depending on the amount of response data calculated, we employ two configurations: *Tier 1* (T1), a coarse-sampling mode for rapid evaluation, and *Tier 2* (T2), a fine-sampling mode for high-fidelity analysis. In the T1 case, we want to infer a first-order qualitative (e.g. positive vs. negative contribution to the output) assessment of the perturbation response for a given wavelength bin. We sample the minimum viable number of points from the response curve and perform linear regression on the resulting perturbation response to acquire the gradient, or the mean posterior response to injected perturbation.

For a specific  $\mathbf{x}_\star$  and  $m$  at T1 the whole pipeline can be condensed into the form  $J_m(\xi_k) = R_k, \forall k \in K$  where  $\xi$  the perturbation is the

drawn from a normal distribution such that  $\xi_k \sim \mathcal{N}_{\text{norm.}}(0, \sigma_m^2)$  and  $\xi \in \mathbb{R}^{1 \times K}$ .

The minimum useful information that we want to extract from this would be to estimate response gradient. This would give us a metric for either positive or negative, as well as scale, of the feature perturbation response. To do this we want to fit the deterministic function  $J_m$  with a linear approximation that is  $J_m(\xi) \approx A\xi$  where  $A$  is the gradient of the linear response approximation (given that  $J_m(\mathbb{R})$  must pass through zero as  $\mathbf{x}' \equiv \mathbf{x}_\star$  where  $\xi_0 = 0$  even if the special case  $\xi_0$  is not in the sampled set  $\xi_0 \notin \xi$ ). To constrain the most efficient way to do this, we must define how many samples  $K$  that we need to constrain our estimation  $\hat{A}$  to within a specific certainty. The minimum  $K$  can be given using

$$K \geq \frac{Z^2 \rho}{\alpha^2}. \quad (21)$$

as shown in [Appendix B](#), where non-linearity coefficient  $\rho = 12\%$  from preliminary studies with an uncertainty  $A \pm \alpha$  where  $\alpha = 10\%$  as a chosen value. To achieve  $2\sigma$  confidence in our response gradient estimate, the minimum number of samples  $K$  which are required is 48. To account for random sample clustering, and ensure that sample density is sufficient, we set a minimum  $K = 50$  samples as the minimum number of samples for the default T1 analysis using PERTURB-c, giving a confidence interval of  $2.0412\sigma$  that the approximation  $\hat{A}$  is within 10% of the true response gradient such that  $(A - \alpha) \leq \hat{A} \leq (A + \alpha)$ . This gives for sufficient accuracy, and ensures repeatability of the method while minimising inference time.

Running PERTURB-c at T1 additionally gives information about the linearity of the feature response in the form of  $\rho_\star$ . For wavelengths which exhibit highly linear perturbation response, any further analysis is unnecessary, however, we find in these trials that this does not represent the majority of wavelength regions.

## 11 TIER 2 ANALYSIS

Given the non-linearity of perturbation response [see [Figure D1](#) and as above], it is not always sufficient to describe feature response as a single response gradient. While PERTURB-c can be used to sample the high resolution response curve of a single input wavelength and visualise this as a *ceteris paribus* style plot, the real power of the framework lies in its ability to visualise the response curves of multiple input wavelengths concurrently. PERTURB-c allows for visualisation of the response gradient per wavelength as a heatmap [[Figure 11](#)]. In order to generate the resolution required for the heatmap, PERTURB-c takes an additional 1,950 samples (for a total of 2,000 samples). This allows for precise visualisation of the model's response curves.

However, this problem with visualisation is also one which affects SHAP, as while SHAP waterfall plots and bar plots are very descriptive for a few discontinuous input features, beyond around five input features, especially with sequential data, they can become difficult and unintuitive to read and the positioning of the bars becomes overall less informative [as in [Figure 5](#)].

In order to overcome this, PERTURB-c heatmap plots [[Figure 12](#)] show the change in model response, or response gradient,  $\delta \mathbf{r}_{m,p} / \delta \xi_m$ . This representation avoids changes in visual weight about the zero horizon (where  $\xi_m = 0$ ) which occur when plotting response *magnitude*, allowing for more intuitive interpretation. Response *magnitude* must pass through zero at zero perturbation, as it is calculated as the difference between the zero-perturbation response

and itself. This means that for any visualisation of response magnitude using a colour-bar scale, as you approaches zero perturbation the information density vanishes to none. Conversely, with response *gradient* there are no such limitations, and changes in gradient values have the same relative visual weight irrespective of perturbation magnitude, making the plots significantly easier to read at a glance. As such, even large numbers of features can be condensed into a single plot using PERTURB-c and still effectively communicate the model response.

## 12 PERTURB-C AS A PROPOSAL TOOL

PERTURB-c can be configured to provide (and visualise) both observational and retrieval constraints for the purposes of rapid prototyping of retrieval observations. Take the desire to investigate a specific hypothesis, such as the existence of tidal heating in the lower atmosphere on our WASP-107b case study. If we know that sulphur only forms  $SO_2$  at temperatures in excess of that at which we expect to see in the upper layers of the atmosphere of WASP-107b, we can generate a forward model as we have done with an atmospheric composition high in  $SO_2$  that would be indicative of significantly higher internal temperatures. Given this forward model as our best case 'observation', we know that in order to robustly prove our hypothesis we must constrain the abundance of  $SO_2$  within a specified uncertainty, say  $^{+15\%}_{-5\%}$ . If we then perform the retrieval on our forward model and then use PERTURB-c to generate response profiles at T2, we can impose  $^{+15\%}_{-5\%}$  limits on the response deviation of  $SO_2$  abundance on a per-wavelength-bin basis, [[Figure 11](#)]. This can inform the number of visits which may be required to constrain the target for this specific hypothesis so that the predicted per-wavelength-bin uncertainties of the instrument fall within the constraints on the retrieved abundance imposed by the hypothesis. Such analysis can also assist with the coordination of multi-instrument synergies so as to effectively fill the spectrum at the required uncertainty level, without requesting telescope time in excess of that required for the proposed hypothesis.

Compliment to this, the method can also be applied in reverse; given the predicted per-wavelength-bin uncertainties of a proposed observation the uncertainty of the retrieved abundance can be estimated, along with the limiting wavelengths at both the positive and negative bounds. This is particularly useful if the instrument is already allocated and the science case and target selection must be shaped around this.

While the methodologies described above do not reflect a high precision analysis of the potential outcomes of any observation, the speed at which they can be performed, and therefore also volume of targets that can be assessed, allows for better allocation of researcher time when it comes to more robust analysis of potential target candidates. This is particularly relevant when looking to fill out mission candidates for specific population level studies aimed at answering a multitude of hypotheses within a single subset of planets. The identification of targets which are interesting because they have potential to answer a multitude of questions makes for a much better sample. However, the identification of these planets manually (while also being particularly labour intensive) can introduce elements of human bias, particularly towards systems which may already be over-observed given the limitations of current analysis techniques, and the use of PERTURB-c at scale mitigates this.

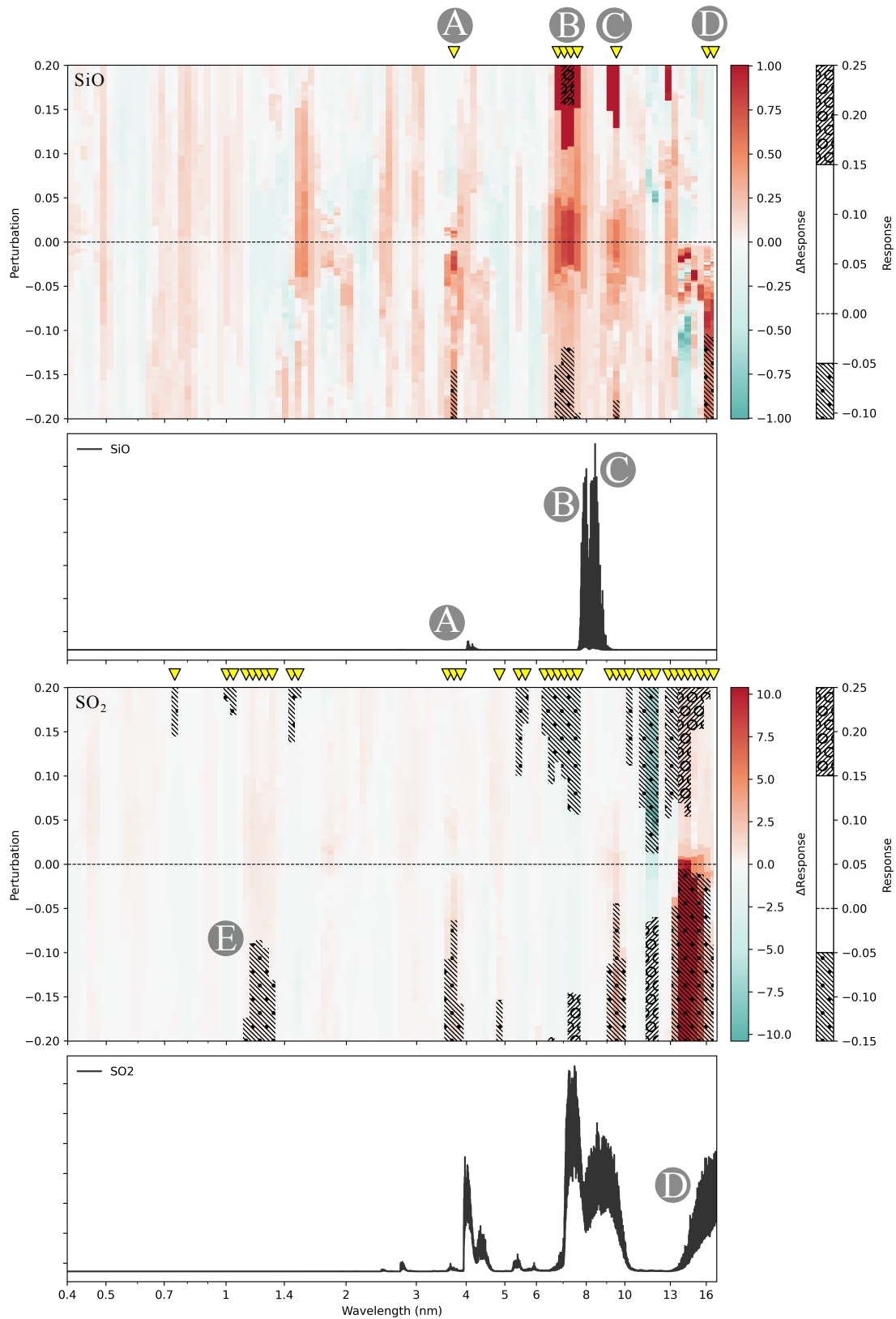


**Figure 11. (overleaf, see page 12)** T2 analysis with PERTURB-c of WASP-107b case study for retrieval of *SiO* (top) and *SO<sub>2</sub>* (lower middle) with  $^{+0.15}_{-0.05}$  abundance uncertainty limits. Molecular contributions for *SiO* (upper middle) and *SO<sub>2</sub>* (bottom) are also shown. For the PERTURB-c heatmaps, yellow markers indicate wavelength bins with active perturbation response limits, i.e. observational uncertainty for these wavelengths needs to be constrained within the non-hatched region in order to achieve target abundance uncertainty. For more detailed explanation of perturbation response limits see Figure 12.

For *SiO* the PERTURB-c heatmap shows the model demonstrates strong agreement with physics based constraints. See regions of positive importance **A**, **B**, and **C**, which correlate with their respective bands in the *SiO*. The **D** region, for which the perturbation response gradient is highly non-linear, corresponds with the respective *SO<sub>2</sub>* band (which is particularly strong in this sample, given the high *SO<sub>2</sub>* abundance), and we hypothesise is being used by the model in order to break the degeneracy between the other *SO<sub>2</sub>* bands and the target molecule *SiO*.

For the *SO<sub>2</sub>* heatmap, the model still demonstrates some agreement with the molecular contribution, but there is much more discrepancy between the two, the most striking of which is in the **E** region. We hypothesise that this corresponds to bands in *H<sub>2</sub>O*, but this connection is tenuous.

Based on these analyses, using an observation of WASP-107b with our hypothetical instrument to constrain the minimum abundance of *SiO* is more plausible than attempting to constrain the minimum abundance of *SO<sub>2</sub>*.

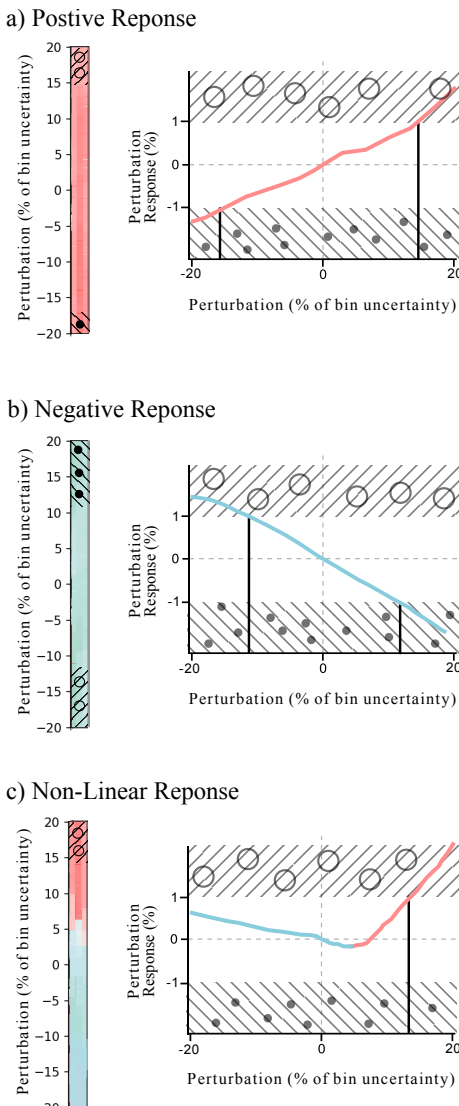


**Figure 12. (left)** Sketch showing how to interpret T2 heatmaps. For each example, the heatmap slice for 3 adjacent wavelength bins is shown along the x heatmap axis. Along the y heatmap axis is the magnitude of perturbation injected, and the colour axis is the rate of change of the perturbation response, the deviation in the model output from the unmodified observation prediction. The right hand plots show the extracted ceteris paribus style curves for the central wavelength in each colour plot. The x axis of the right hand plots correlates with the y axis of the heatmaps. The hatched regions show upper and lower perturbation response limits in the retrieved abundance on the right, and denote when the response curve crosses into these regions in the bars on the left. These can be asymmetric but for this example are set to  $\pm 1\%$  of the perturbation response.

For the **a)** example the model response is positive, this means that any deviation for this wavelength bin is positively correlated with the model prediction for this molecular abundance. The response crosses outside of the permitted upper and lower limits at  $+15\%$  and  $-18\%$  uncertainty deviation respectively. As such, for the desired constraint on the retrieved abundance, the observation uncertainty can be at a maximum  $x^{+0.15}_{-0.18}$ .

Likewise for the **b)** example, the correlation is negative. As such high positive deviation causes the response to cross the lower limit and vice versa. To satisfy the desired constraint on the retrieved abundance, the observation uncertainty for this wavelength bin can be at a maximum  $x^{+0.11}_{-0.12}$ .

In the case of the **c)** example, the response is non-linear. Any deviation in the input wavelength bin results in an increase in the predicted abundance. There are many different types of non-linear responses, but this (or its inverse about  $y=0$ : any deviation results in decrease) are the most commonly seen at the edges (or regions with low deviation across the sample set) as they correspond with the wavelength bin being used to set upper or lower limits to scale the sample. More complex correlations should be treated with caution as they likely represent deviation outside of the model training distribution and suggest that the instrument noise is too large for the width of the training distribution, or more plainly, the exploration of upper or lower uncertainty limits is carrying the observation outside of the limits of the training data, resulting in unstable prediction. As in this case, the response does not necessarily always cross the set thresholds, as such the lower limit on uncertainty at this wavelength bin in observation is at most constrained by the limit of the perturbation we tested, but could be lower.

### 13 CONCLUSIONS

This work begins to unpack some of the issues with existing retrieval frameworks, but is by no means a comprehensive rebuttal of the techniques, or even proposes an exhaustive successor. This being said as both the volume and resolution of data increases, and as we begin to ask more complex questions about distant worlds, it is clear to see that there is a need, if not even inevitably so, for some combination of machine learning alongside Bayesian retrieval frameworks in the future of retrievals. As such, we have a long way to go in the exploration of suitable interpretability metrics to describe our confidence in the ‘reasoning’ of these methods in a similar vein to Bayesian posterior density and evidence. Beginning to explore ways by which we can mitigate or circumnavigate the complex effects of the correlation which is so prevalent within spectral data marks a crucial step in the direction towards transparency in machine learning retrieval frameworks.

The experiments outlined here and the PERTURB-c framework seek to contribute to this. We show proof for the correlated nature of spectral observations, and characterise this anecdotally as approximately Gaussian in relation to wavelength separation. We mathematically demonstrate the weakness of existing *ceteris paribus* and SHAP methods to correlation of this nature; their propensity to generate out of distribution samples is driven at their core by their purely stochastic sample generation techniques, which do not account for inherent *intraspot* correlation. We then propose PERTURB-c, which is far more robust to this by application of the aforementioned Gaussian *intraspot* correlation approximation. We demonstrate the application of these techniques on a case study based on WASP-107b, and successfully retrieve the high  $SO_2$  concentrations present using machine learning architecture from Clarke et al. (2026). Critically, we are then able to explain these predictions, in tandem with predictions of  $SiO$  using PERTURB-c, attributing high feature importance to regions where  $SiO$  and  $SO_2$  spectral features are present in accordance with the molecular contributions from which the original simulated observation was derived, even going as far as to infer ways in which the model has learned to break degeneracy between these two molecular species. In addition to this, we were able to do so at 1/10th of the latency of SHAP analysis due to the sample efficiency of the PERTURB-c method. We present the resulting interpretability as a novel visualisation which we hope is more intuitive than standard SHAP feature importance visualisations in conveying the information given the large number of input features.

To conclude, we hope PERTURB-c in its current form will provide utility to those who seek to make fast synthetic retrievals for the verification of observational strategy and in the preparation of telescope proposals, and to lay the groundwork for further exploration into how we can collectively improve confidence and cohesion in our retrieval strategies going forward in supporting the population level studies of the future.

### ACKNOWLEDGEMENTS

With thanks to Sushuang Ma for work in preparing the planet dataset, Jack Davey for help in preparing the binning grid, and Sergey Yurchenko and everyone at the ExoMol team for preparing the line lists used in generating molecular contributions.

### DATA AVAILABILITY

We hope to release PERTURB-c as a package alongside this publication; the most up-to-date implementation of which is available at <https://joolsclarke.co.uk/perturb>. The Ariel Data Challenge dataset is publicly available at <https://huggingface.co/datasets/n1ghtf411/Ariel-Data-Challenge-NeurIPS-2022>. Code implementing the methods as they are described in this paper can be found at [https://joolsclarke.co.uk/perturb/perturb-c\\_2025/code](https://joolsclarke.co.uk/perturb/perturb-c_2025/code), and the dataset of simulated observations will be made available at [https://joolsclarke.co.uk/perturb/perturb-c\\_2025/dataset](https://joolsclarke.co.uk/perturb/perturb-c_2025/dataset). Access to molecular contribution data can be provided upon request.

This paper has been typeset from a  $\text{\TeX}$ / $\text{\LaTeX}$  file prepared by the author.

### REFERENCES

Al-Refaie, A. F., Changeat, Q., Waldmann, I. P., & Tinetti, G., 2021. Tau-REX III: A fast, dynamic and extendable framework for retrievals, *The Astrophysical Journal*, **917**(1), 37.

Azzam, A. A. A., Tennyson, J., Yurchenko, S. N., & Naumenko, O. V., 2016. ExoMol molecular line lists – XVI. The rotation–vibration spectrum of hot  $H_2S$ , *Monthly Notices of the Royal Astronomical Society*, **460**(4), 4063–4074.

Barstow, J. K., Aigrain, S., Irwin, P. G. J., & Sing, D. K., 2016. A Consistent Retrieval Analysis of 10 hot Jupiters Observed in Transmission, *The Astrophysical Journal*, **834**(1), 50.

Barstow, J. K., Changeat, Q., Garland, R., Line, M. R., Rocchetto, M., & Waldmann, I. P., 2020. A comparison of exoplanet spectroscopic retrieval tools, *Monthly Notices of the Royal Astronomical Society*, **493**(4), 4884–4909.

Bashi, D., Helled, R., & Zucker, S., 2018. A Quantitative Comparison of Exoplanet Catalogs, *Geosciences*, **8**(9), 325.

Bell, T. J., Ahrer, E.-M., Brande, J., Carter, A. L., Feinstein, A. D., Caloca, G. G., Mansfield, M., Zieba, S., Piaulet, C., Benneke, B., et al., 2022. Eureka!: An End-to-End Pipeline for JWST Time-Series Observations, *Journal of Open Source Software*, **7**(79), 4503.

Benneke, B., Wong, I., Piaulet, C., Knutson, H. A., Lothringer, J., Morley, C. V., Crossfield, I. J. M., Gao, P., Greene, T. P., Dressing, C., et al., 2019. Water Vapor and Clouds on the Habitable-zone Sub-Neptune Exoplanet K2-18b, *The Astrophysical Journal*, **887**, L14.

Bicek, P. & Burzykowski, T., 2021. *Explanatory Model Analysis*, Chapman and Hall/CRC, New York.

Bowesman, C. A., Qu, Q., McKemmish, L. K., Yurchenko, S. N., & Tennyson, J., 2024. ExoMol line lists – LV: Hyperfine-resolved molecular line list for vanadium monoxide (51V16O), *Monthly Notices of the Royal Astronomical Society*, **529**(2), 1321–1332.

Buldyrev, J., Stehlin, K., Yurchenko, S. N., Guest, E. R., & Tennyson, J., 2025. Semiclassical Estimates of Pressure-induced Line Widths for Infrared Absorption in Hot (Exo)planetary Atmospheres, *The Astrophysical Journal Supplement Series*, **276**(1), 23.

Charbonneau, D., Brown, T. M., Latham, D. W., & Mayor, M., 1999. Detection of Planetary Transits Across a Sun-like Star, *The Astrophysical Journal*, **529**(1), L45.

Chubb, K. L., Rocchetto, M., Yurchenko, S. N., Min, M., Waldmann, I., Barstow, J. K., Mollière, P., Al-Refaie, A. F., Phillips, M. W., & Tennyson, J., 2021. The ExoMolOP database: Cross sections and k-tables for molecules of interest in high-temperature exoplanet atmospheres, *Astronomy & Astrophysics*, **646**, A21.

Clarke, J. D., Yip, G., & Nikolaou, N., 2026. Posterior quantification in non-stochastic machine learning retrievals, Manuscript in preparation.

Cobb, A. D., Himes, M. D., Soboczenski, F., Zorzan, S., O’Beirne, M. D., Baydin, A. G., Gal, Y., Domagal-Goldman, S. D., Arney, G. N., & Anger

hausen, D., 2019. An Ensemble of Bayesian Neural Networks for Exo-planetary Atmospheric Retrieval, *The Astronomical Journal*, **158**(1), 33.

Coles, P. A., Yurchenko, S. N., & Tennyson, J., 2019. ExoMol molecular line lists – XXXV. A rotation-vibration line list for hot ammonia, *Monthly Notices of the Royal Astronomical Society*, **490**(4), 4638–4647.

Cowan, N. B., Greene, T., Angerhausen, D., Batalha, N. E., Clampin, M., Colon, K., Crossfield, I. J. M., Fortney, J. J., Gaudi, B. S., Harrington, J., et al., 2015. Characterizing Transiting Planet Atmospheres through 2025, *Publications of the Astronomical Society of the Pacific*, **127**(949), 311–327.

Dyrek, A., Min, M., Decin, L., Bouwman, J., Crouzet, N., Mollière, P., Lagage, P.-O., Konings, T., Tremblin, P., Güdel, M., et al., 2024. SO<sub>2</sub>, silicate clouds, but no CH<sub>4</sub> detected in a warm Neptune, *Nature*, **625**(7993), 51–54.

Edwards, B. & Tinetti, G., 2022. The Ariel Target List: The Impact of TESS and the Potential for Characterising Multiple Planets Within a System, *The Astronomical Journal*, **164**(1), 15.

Espinoza, N., Rackham, B. V., Jordán, A., Apai, D., López-Morales, M., Osip, D. J., Grimm, S. L., Hoeijmakers, J., Wilson, P. A., Bixel, A., et al., 2019. ACCESS: A featureless optical transmission spectrum for WASP-19b from Magellan/IMACS, *Monthly Notices of the Royal Astronomical Society*, **482**(2), 2065–2087.

Feroz, F., Hobson, M. P., & Bridges, M., 2009. MultiNest: An efficient and robust Bayesian inference tool for cosmology and particle physics, *Monthly Notices of the Royal Astronomical Society*, **398**(4), 1601–1614.

Figueroa, R. L., Zeng-Treitler, Q., Kandula, S., & Ngo, L. H., 2012. Predicting sample size required for classification performance, *BMC Medical Informatics and Decision Making*, **12**(1), 8.

Fisher, C. & Heng, K., 2022. How do we optimally sample model grids of exoplanet spectra?, *The Astrophysical Journal*, **934**(1), 31.

Fisher, C., Hoeijmakers, H. J., Kitzmann, D., Márquez-Neila, P., Grimm, S. L., Sznitman, R., & Heng, K., 2020. Interpreting High-Resolution Spectroscopy of Exoplanets Using Cross-Correlations and Supervised Machine Learning, *The Astronomical Journal*, **159**(5), 192.

Foreman-Mackey, D., Hogg, D. W., Lang, D., & Goodman, J., 2013. Emcee: The MCMC Hammer, *Publications of the Astronomical Society of the Pacific*, **125**(925), 306–312.

Gardner, J. P., Mather, J. C., Abbott, R., Abell, J. S., Abernathy, M., Abney, F. E., Abraham, J. G., Abraham, R., Abul-Huda, Y. M., Acton, S., et al., 2023. The James Webb Space Telescope Mission, *Publications of the Astronomical Society of the Pacific*, **135**(1048), 068001.

Guest, E. R., Tennyson, J., & Yurchenko, S. N., 2024. Predicting the rotational dependence of line broadening using machine learning, *Journal of Molecular Spectroscopy*, **401**, 111901.

Haswell, C. A., 2010. *Transiting Exoplanets*, Cambridge University Press.

Huang, X. & Marques-Silva, J., 2023. The Inadequacy of Shapley Values for Explainability.

Lueber, A., Karchev, K., Fisher, C., Heim, M., Trotta, R., & Heng, K., 2025. Near-instantaneous Atmospheric Retrievals and Model Comparison with FASTER.

Lundberg, S. & Lee, S.-I., 2017. A Unified Approach to Interpreting Model Predictions.

Lustig-Yaeger, J., Fu, G., May, E. M., Ceballos, K. N. O., Moran, S. E., Peacock, S., Stevenson, K. B., Kirk, J., López-Morales, M., MacDonald, R. J., et al., 2023. A JWST transmission spectrum of the nearby Earth-sized exoplanet LHS 475 b, *Nature Astronomy*, **7**, 1317–1328.

Ma, S., Ito, Y., Al-Refaie, A. F., Changeat, Q., Edwards, B., & Tinetti, G., 2023. YunMa: Enabling Spectral Retrievals of Exoplanetary Clouds, *The Astrophysical Journal*, **957**(2), 104.

MacDonald, R. J. & Batalha, N. E., 2023. A Catalogue of Exoplanet Atmospheric Retrieval Codes, *Research Notes of the AAS*, **7**(3), 54.

Madhusudhan, N., Sarkar, S., Constantinou, S., Holmberg, M., Piette, A. A., & Moses, J. I., 2023. Carbon-bearing Molecules in a Possible Hycean Atmosphere, *The Astrophysical Journal*, **956**, L13.

Márquez-Neila, P., Fisher, C., Sznitman, R., & Heng, K., 2018. Supervised machine learning for analysing spectra of exoplanetary atmospheres, *Nature Astronomy*, **2**(9), 719–724.

Martinez, F. A., Min, M., Kamp, I., & Palmer, P. I., 2022. Convolutional neural networks as an alternative to Bayesian retrievals, *Astronomy & Astrophysics*, **662**, A108.

Mase, M., Owen, A. B., & Seiler, B., 2020. Explaining black box decisions by Shapley cohort refinement.

McKemmish, L. K., Masseron, T., Hoeijmakers, H. J., Pérez-Mesa, V., Grimm, S. L., Yurchenko, S. N., & Tennyson, J., 2019. ExoMol molecular line lists – XXXIII. The spectrum of Titanium Oxide, *Monthly Notices of the Royal Astronomical Society*, **488**(2), 2836–2854.

Medova, E., 2014. Bayesian Analysis and Markov Chain Monte Carlo Simulation, in *Encyclopedia of Quantitative Risk Analysis and Assessment*, John Wiley & Sons, Ltd.

Molnar, C., 2018. *Interpretable Machine Learning (Third Edition)*, Leanpub.

Mugnai, L. V., Al-Refaie, A., Bocchieri, A., Changeat, Q., Pascale, E., & Tinetti, G., 2021. Alfnoor: Assessing the Information Content of Ariel's Low-resolution Spectra with Planetary Population Studies, *The Astronomical Journal*, **162**(6), 288.

National Academies of Sciences, Engineering, and Medicine, 2018. *Exoplanet Science Strategy*, National Academies Press, Washington, D.C.

Ng, W. Y., Wang, L. R., Liu, S., & Fan, X., 2025. Causal SHAP: Feature Attribution with Dependency Awareness through Causal Discovery.

Nixon, M. C. & Madhusudhan, N., 2020. Assessment of Supervised Machine Learning for Atmospheric Retrieval of Exoplanets, *Monthly Notices of the Royal Astronomical Society*, **496**(1), 269–281.

Pinhas, A., Madhusudhan, N., Gandhi, S., & MacDonald, R., 2019. H2O abundances and cloud properties in ten hot giant exoplanets, *Monthly Notices of the Royal Astronomical Society*, **482**(2), 1485–1498.

Polyansky, O. L., Kyuberis, A. A., Zobov, N. F., Tennyson, J., Yurchenko, S. N., & Lodi, L., 2018. ExoMol molecular line lists XXX: A complete high-accuracy line list for water, *Monthly Notices of the Royal Astronomical Society*, **480**(2), 2597–2608.

Rustamkulov, Z., Sing, D. K., Liu, R., & Wang, A., 2022. Analysis of a JWST NIRSpec Lab Time Series: Characterizing Systematics, Recovering Exoplanet Transit Spectroscopy, and Constraining a Noise Floor, *The Astrophysical Journal Letters*, **928**(1), L7.

Seager, S. & Deming, D., 2010. Exoplanet Atmospheres, *Annual Review of Astronomy and Astrophysics*, **48**(Volume 48, 2010), 631–672.

Sedaghati, E., Boffin, H. M. J., MacDonald, R. J., Gandhi, S., Madhusudhan, N., Gibson, N. P., Oshagh, M., Claret, A., & Rauer, H., 2017. Detection of titanium oxide in the atmosphere of a hot Jupiter, *Nature*, **549**(7671), 238–241.

Sing, D. K., Fortney, J. J., Nikolov, N., Wakeford, H. R., Kataria, T., Evans, T. M., Aigrain, S., Ballester, G. E., Burrows, A. S., Deming, D., et al., 2016. A continuum from clear to cloudy hot-Jupiter exoplanets without primordial water depletion, *Nature*, **529**(7584), 59–62.

Sousa-Silva, C., Al-Refaie, A. F., Tennyson, J., & Yurchenko, S. N., 2015. ExoMol line lists – VII. The rotation–vibration spectrum of phosphine up to 1500 K, *Monthly Notices of the Royal Astronomical Society*, **446**(3), 2337–2347.

Speagle, J. S., 2020. Dynesty: A Dynamic Nested Sampling Package for Estimating Bayesian Posteriors and Evidences, *Monthly Notices of the Royal Astronomical Society*, **493**(3), 3132–3158.

Štrumbelj, E. & Kononenko, I., 2014. Explaining prediction models and individual predictions with feature contributions, *Knowledge and Information Systems*, **41**(3), 647–665.

Tahseen, T. P. A., Mendonça, J. M., Yip, K. H., & Waldmann, I. P., 2024. Enhancing 3D Planetary Atmosphere Simulations with a Surrogate Radiative Transfer Model, *Monthly Notices of the Royal Astronomical Society*, **535**(3), 2210–2227.

Tahseen, T. P. A., Simões, L. F., Yip, K. H., Nikolaou, N., Mendonça, J. M., & Waldmann, I. P., 2025. Extreme Learning Machines for Exoplanet Simulations: A Faster, Lightweight Alternative to Deep Learning.

Tennyson, J. & Yurchenko, S. N., 2018. The ExoMol Atlas of Molecular Opacities, *Atoms*, **6**(2), 26.

Thompson, A., Biagini, A., Cracchiolo, G., Petralia, A., Changeat, Q., Saba, A., Morello, G., Morvan, M., Micela, G., & Tinetti, G., 2023. Correcting Exoplanet Transmission Spectra for Stellar Activity with an Optimised Retrieval Framework.

Tinetti, G., Eccleston, P., Haswell, C., Lagage, P.-O., Leconte, J., Lüftinger,

T., Micela, G., Min, M., Pilbratt, G., Puig, L., et al., 2021. Ariel: Enabling planetary science across light-years.

Tsiaras, A., Waldmann, I. P., Tinetti, G., Tennyson, J., & Yurchenko, S. N., 2019. Water vapour in the atmosphere of the habitable-zone eight-Earth-mass planet K2-18 b, *Nature Astronomy*, **3**, 1086–1091.

Underwood, D. S., Tennyson, J., Yurchenko, S. N., Huang, X., Schwenke, D. W., Lee, T. J., Clausen, S., & Fateev, A., 2016. ExoMol molecular line lists – XIV. The rotation–vibration spectrum of hot SO<sub>2</sub>, *Monthly Notices of the Royal Astronomical Society*, **459**(4), 3890–3899.

Weber, R. O., Johs, A. J., Goel, P., & Silva, J. M., 2024. XAI is in trouble, *AI Magazine*, **45**(3), 300–316.

Welbanks, L., McGill, P., Line, M., & Madhusudhan, N., 2023. On the Application of Bayesian Leave-one-out Cross-validation to Exoplanet Atmospheric Analysis, *The Astronomical Journal*, **165**(3), 112.

Welbanks, L., Nixon, M. C., McGill, P., Tilke, L. J., Wiser, L. S., Rotman, Y., Mukherjee, S., Feinstein, A., Line, M. R., Benneke, B., et al., 2025. Challenges in the detection of gases in exoplanet atmospheres, *Nature Astronomy*.

Yip, K. H., Changeat, Q., Nikolaou, N., Morvan, M., Edwards, B., Waldmann, I. P., & Tinetti, G., 2021. Peeking inside the Black Box: Interpreting Deep Learning Models for Exoplanet Atmospheric Retrievals.

Yip, K. H., Waldmann, I. P., Changeat, Q., Morvan, M., Al-Refaie, A. F., Edwards, B., Nikolaou, N., Tsiaras, A., de Oliveira, C. A., Lagage, P.-O., Jenner, C., Cho, J. Y.-K., Thiyagalingam, J., & Tinetti, G., 2022. ESA-Ariel Data Challenge NeurIPS 2022: Inferring Physical Properties of Exoplanets From Next-Generation Telescopes.

Yip, K. H., Changeat, Q., Al-Refaie, A., & Waldmann, I., 2023. To Sample or Not To Sample: Retrieving Exoplanetary Spectra with Variational Inference and Normalising Flows.

Yurchenko, S. N., Tennyson, J., Syme, A.-M., Adam, A. Y., Clark, V. H. J., Cooper, B., Dobney, C. P., Donnelly, S. T. E., Gorman, M. N., Lynas-Gray, A. E., Meltzer, T., Owens, A., Qu, Q., Semenov, M., Somogyi, W., Upadhyay, A., Wright, S., & Zapata Trujillo, J. C., 2022. ExoMol line lists – XLIV. Infrared and ultraviolet line list for silicon monoxide (28Si16O), *Monthly Notices of the Royal Astronomical Society*, **510**(1), 903–919.

Yurchenko, S. N., Owens, A., Kefala, K., & Tennyson, J., 2024. ExoMol line lists – LVII. High accuracy ro-vibrational line list for methane (CH<sub>4</sub>), *Monthly Notices of the Royal Astronomical Society*, **528**(2), 3719–3729.

Yurchenko, S. N., Barnfield, M. G., Bowesman, C. A., Brady, R. P., Guest, E. R., Kefala, K., Ni, Q.-H., Perri, A. N., Smola, O. A., Solokov, A., Tao, C., & Tennyson, J., 2026. ExoMol line lists – LXIII. ExoMol line lists for 12 isotopologues of CO<sub>2</sub>, *Monthly Notices of the Royal Astronomical Society*, **545**(3), staf2135.

Zingales, T. & Waldmann, I. P., 2018. ExoGAN: Retrieving Exoplanetary Atmospheres Using Deep Convolutional Generative Adversarial Networks, *The Astronomical Journal*, **156**(6), 268.

## APPENDIX A: BRIEF OVERVIEW OF EXOPLANET OBSERVATION STRATEGY

The first transit observations were performed by ground based wide-field telescopes (Charbonneau et al. 1999); because they were only looking for dimming effects in white light, they could survey multiple stars simultaneously over long time periods. In the modern era transit observations are taken using space-based instruments which target a single stellar host with a spectrograph when the planet is in transit, according to a pre-calculated ephemeris. As such the raw data collected by transit observations is *luminosity per wavelength over time*. The time component of these observations can be removed by a data reduction (Bell et al. 2022) to produce a fixed spectrum, which represents the idealised mid-transit where the planet and star are in exact syzygy with the observer and appear as concentric disks. As such the units with which we describe luminosity in these observations are  $(r_{\text{planet}}/r_{\text{star}})^2$  where  $r$  is radius. This observation is consistent with a 1D snapshot of a globally homogeneous atmosphere at the terminator (sunrise on one half of the planet's circumference, and sunset for the other) (Haswell 2010). From this, the molecular composition of the atmosphere can be estimated, based on the spectral absorption properties of different molecular species which can be calculated through a combination of laboratory experiments and ab-initio calculation (Tennyson & Yurchenko 2018).

Both the volume and quality of transit data recorded has been rapidly increasing, and with the advent of JWST (Gardner et al. 2023) and now the upcoming Ariel mission (Tinetti et al. 2021), this trend stands to continue (Lustig-Yaeger et al. 2023). These missions, and others like them over the coming years, will deliver unprecedented quantity and quality of spectral data of this nature, allowing for characterisation of a significantly larger percentage of the now detected planets (Edwards & Tinetti 2022), but also characterisation in much more detail of those which have already been studied (Tsiaras et al. 2019; Benneke et al. 2019; Madhusudhan et al. 2023)<sup>10</sup>. This creates both opportunity and challenge for the field: the wealth of new data will facilitate better understanding at a population level, allowing us to study planets in the context of a wider sample, however, analysis methods must scale efficiently in order to manage this magnitude of data.

The current gold standard for interpreting exoplanet observations is iterative optimisation of the inverse problem. It is much less complex to simulate a transit observation given parameters about the system than it is to infer these system parameters from an observation. A forward model is a physics-driven atmospheric model capable of taking a set of planetary and system parameters and producing a simulated observation for this hypothetical scenario (Al-Refaei et al. 2021). By treating the problem as one of optimisation, the input parameters (planetary temperature, molecular abundances, cloud height, etc.) can be iterated so that a forward model of the simulated transit spectrum matches as closely as possible to observational data. However this approach can be computationally intensive. Although the simplest of forward models are relatively lightweight, adding accurate cloud simulations increases physical accuracy at the cost of model complexity Ma et al. (2023), while including additional molecules increases comprehensivity at the expense of the number of parameters to optimise (Welbanks et al. 2025). Both of these factors have compounding impact on forward model inference speed. Furthermore, including additional molecules not only increases the complexity of the problem, but also the risk of multiple degenerate solutions.

In order to minimise the number of calls to the forward model needed for convergence, the typical framework used is Markov Chain Monte Carlo (MCMC) Bayesian minimisation (Medova 2014; Haswell 2010). This selects sample parameters to gain the most new information about the parameter space possible per sample, and can converge on a local minimum (where the residuals between the observation and the simulation are small) much faster than a naïve search approach.

<sup>10</sup> If we take K2-18 b as an example, in Tsiaras et al. (2019) a total of 17 datapoints are recorded from Hubble WFC3, later in Benneke et al. (2019) it is 20 datapoints total - 17 from Hubble WFC3, 1 from Kepler and 2 from Spitzer IRAC, yet with the launch of JWST we see Madhusudhan et al. (2023) where 4411 datapoints are recorded, 1010 from JWST NIRISS and 3401 from JWST NIRSpec.

However, the field is shifting towards the use of nested sampling as a minimiser instead despite its worse convergence speed with large numbers of free parameters, as it has better performance across multiple degenerate solutions due to its ability to navigate multiple local minima concurrently, e.g. TauReX (Al-Refaei et al. 2021). While MCMC explores the parameter space as a single agent in a random walk fashion, nested sampling handles a set of live points concurrently which effectively map the whole surface into a series of shells that can converge on multiple islands of solutions. On top of this, nested sampling provides *Bayesian evidence*, which is a useful metric for native model comparison.

(Discussion continues in Section 2.1.)

## APPENDIX B: T1 PROSPECTIVE POWER ANALYSIS DERIVATION

To begin we note how we define the 'fit' to the linear approximation of this using the sum of squared residuals, in other words

$$\text{RSS} = \sum_k [\hat{A}\xi_k - R_k]^2, \quad (\text{B1})$$

where  $\hat{A}$  is the estimated gradient coefficient. This allows us to set out optimal value for the coefficient  $A$  such that

$$\begin{aligned} A &= \arg \min_{\hat{A}} \mathbb{E}_{\xi} [(\hat{A}\xi_k - R_k)^2] \\ &= \frac{\mathbb{E}[\xi_k R_k]}{\mathbb{E}[\xi_k^2]} \\ &= \frac{1}{\sigma_m^2} \mathbb{E}[\xi_k R_k] \end{aligned} \quad (\text{B2})$$

as we define  $\xi_k \sim \mathcal{N}_{\text{norm.}}(0, \sigma_m)$ , then  $\mathbb{E}[\xi_k^2] = \sigma_m^2$ . By taking  $K$  samples then, the estimate  $\hat{A}$  becomes

$$\hat{A} = \frac{\sum_{k=1}^K \xi_k R_k}{\sum_{k=1}^K \xi_k^2}. \quad (\text{B3})$$

As such we can see the uncertainty in  $\hat{A}$  scales with  $\frac{1}{K\sigma_m^2}$ . We know from above that increasing  $\sigma_m$  only results in poorer information quality, as the number of likely physical samples in the training dataset at high variances becomes diminishing. Furthermore, the linearity of the model response (likely as a result of the former) degrades as variance increases. As such we implicitly can express  $J(\xi)$  as the Taylor expansion  $a\xi + b\xi^2 + c\xi^3 + \dots O^4$  in which we are only interested in  $a$ , and the rest of the terms can be bundled into a residual such that

$$J_{n,m}(\xi) = A\xi + \delta(\xi). \quad (\text{B4})$$

Therefore the estimation error in our above model is given by

$$\hat{A} - A = \frac{\sum_{k=1}^K \xi_k \times \delta(\xi_k)}{\sum_{k=1}^K \xi_k^2}. \quad (\text{B5})$$

We take the expected variance for  $\delta(\xi_k)$  to be  $\sigma_{\delta}^2$ , which gives us our variance in  $\hat{A}$  relative to  $\xi$  as

$$\text{Var}(\hat{A}|\xi) = \frac{\sigma_{\delta}^2}{\sum_{k=1}^K \xi_k^2}, \quad (\text{B6})$$

and given  $\xi_k \sim \mathcal{N}_{\text{norm.}}(0, \sigma_m^2)$ , the variance of  $\hat{A}$  independent of  $\xi_k$  is given by

$$\text{Var}(\hat{A}) = \frac{\sigma_{\delta}^2}{K\sigma_m^2}. \quad (\text{B7})$$

Having satisfied ourselves that minimising the uncertainty in  $A$  is best achieved by an increase in  $K$ , lets define an 'acceptable' approximation for  $A$  and quantify the required  $K$  for  $\hat{A}$  to meet this criterion

Across the preliminary testing (under assumptions from Yip et al. (2022)

using simplified variation of model from [Clarke et al. \(2026\)](#) that we performed, the response curve was prone to a minor positive inflection about  $\xi_k = 0$ . If we take the residual variance relative to the signal variance, it is a reasonable assumption based on preliminary experiments that the non-linear portion of the model contributes to below 12% of the variance of the linear portion, which we then define as

$$\rho \equiv \frac{\sigma_\delta^2}{\text{Var}(A\xi)} = 12\%. \quad (\text{B8})$$

We must tolerate some error in our approximation, to account for the sample mismatch between our assumed linear approximation and the non-linear response, which we will constrain such that as

$$\alpha \geq \frac{|\hat{A} - A|}{|A|} = 10\%. \quad (\text{B9})$$

To achieve  $2\sigma$  confidence in our response gradient estimate, the minimum number of samples  $K$  which are required is then

$$K \geq \frac{Z^2 \rho}{\alpha^2} = \frac{2^2 \times 0.12}{0.1^2} = 48, \quad (\text{B10})$$

as in [Equation 21](#).

## APPENDIX C: SPECTRAL CORRELATION

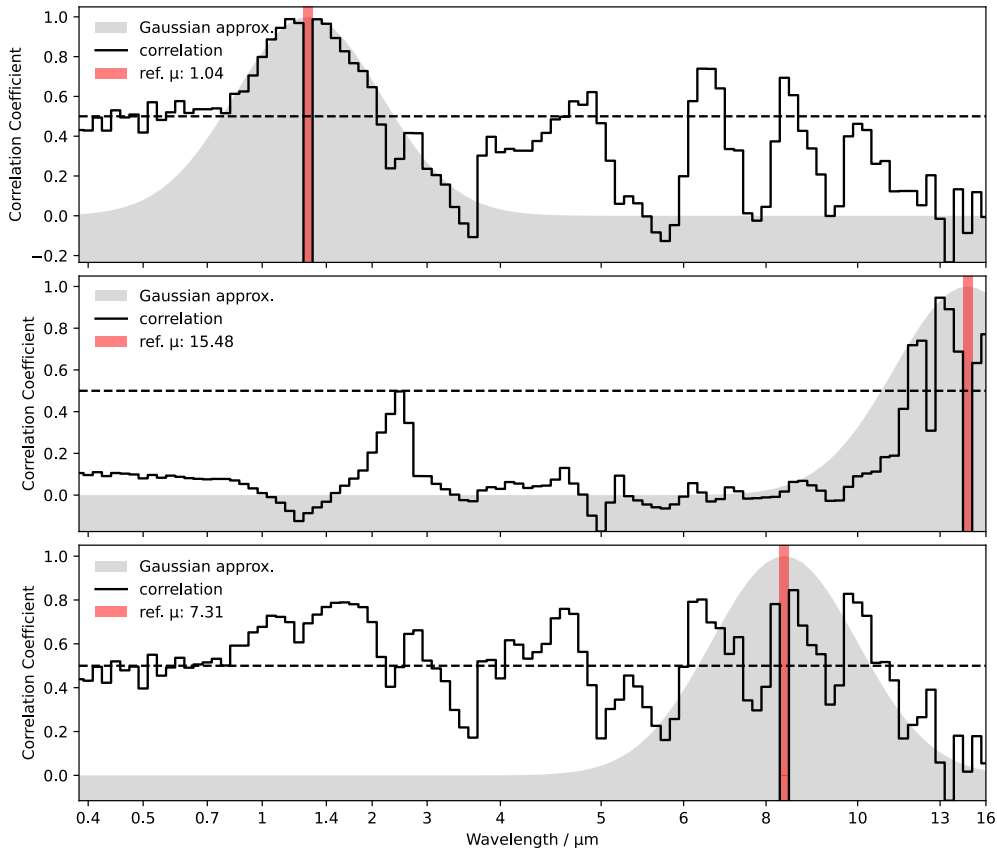


**Figure C1.** Examples of intra-spectral correlation within the training dataset. **(Top)** Example of a well correlated wavelength that follows the Gaussian approximation. **(Middle)** Example of a relatively well correlated wavelength, this is representative of the level of agreement with the Gaussian approximation that the majority of wavelengths exhibit. **(Bottom)** Example of a poorly correlated wavelength. Some wavelengths exhibit seeming very little proximity correlation. This accounts for around 10% of wavelengths, all of which are in this region. Overall, it is a reasonable to assume this Gaussian approximation in order to make physically motivated perturbations providing that the perturbation magnitude remains small (at least half an order of magnitude smaller) compared with the total magnitude.

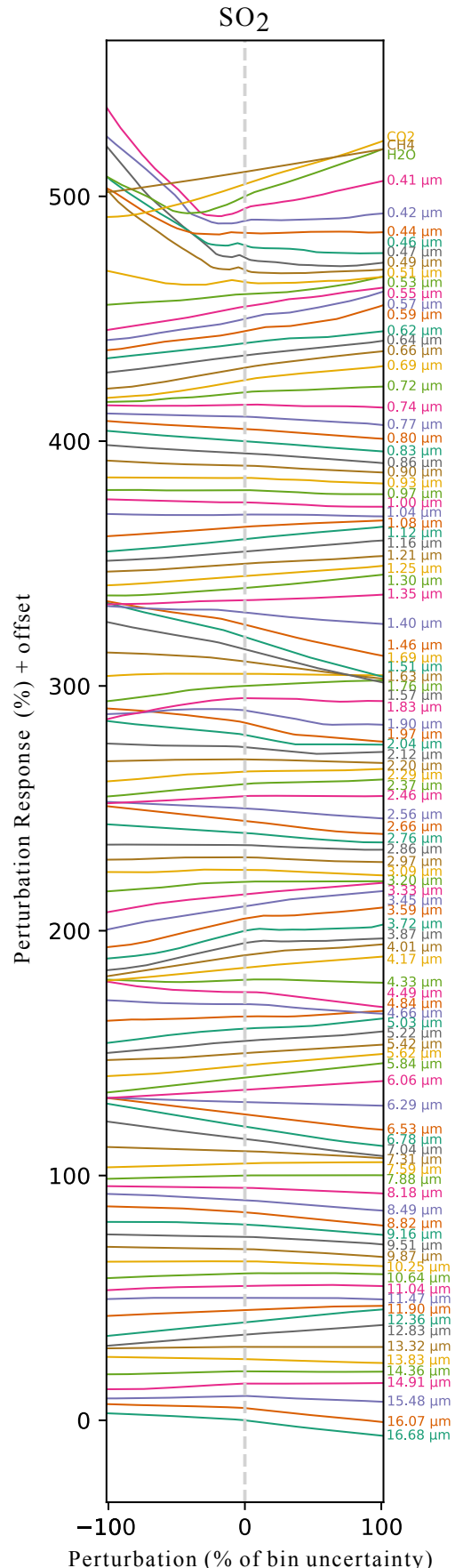
## APPENDIX D: EXTENDED CETERIS PARIBUS

**Figure D1. (right)** Perturbation response for the prediction of  $SO_2$  in WASP-107b case study sample, shown as ceteris paribus style response curves. Perturbation magnitude as a factor of bin uncertainty is shown along the x axis, with response as a factor of unmodified prediction shown on the y axis, with an offset of 5% for clarity. Each curve is labelled by the central wavelength of the Gaussian mask. The top three curves show the ceteris paribus influence for the priors for  $H_2O$ ,  $CO_2$ , and  $CH_4$ .

## APPENDIX E: TRAINING DATASET

Parameter	Unit	Minimum Value	Maximum Value
$H_2O$	log abundance	-10	-3
$CO_2$	log abundance	-10	-3
$CH_4$	log abundance	-10	-3
$NH_3$	log abundance	-10	-5
$H_2S$	log abundance	-10	-5
$PH_3$	log abundance	-10	-5
$SO_2$	log abundance	-10	-5
$SiO$	log abundance	-10	-5
$TiO$	log abundance	-10	-5
$VO$	log abundance	-10	-6
Cloud Pressure	log bar	-5	-1

**Figure E1. (above)** This table shows the ranges of atmospheric values for the training dataset. For the ‘common’ molecules in the upper section ( $H_2O$ ,  $CO_2$ ,  $PH_3$ ) the model was provided priors during training, and the performance of the model is assessed only on the more ‘interesting’ and exotic molecules in the lower section, as these have far more complex and interesting spectral signatures. The full distribution is visualised in [Figure E2](#).



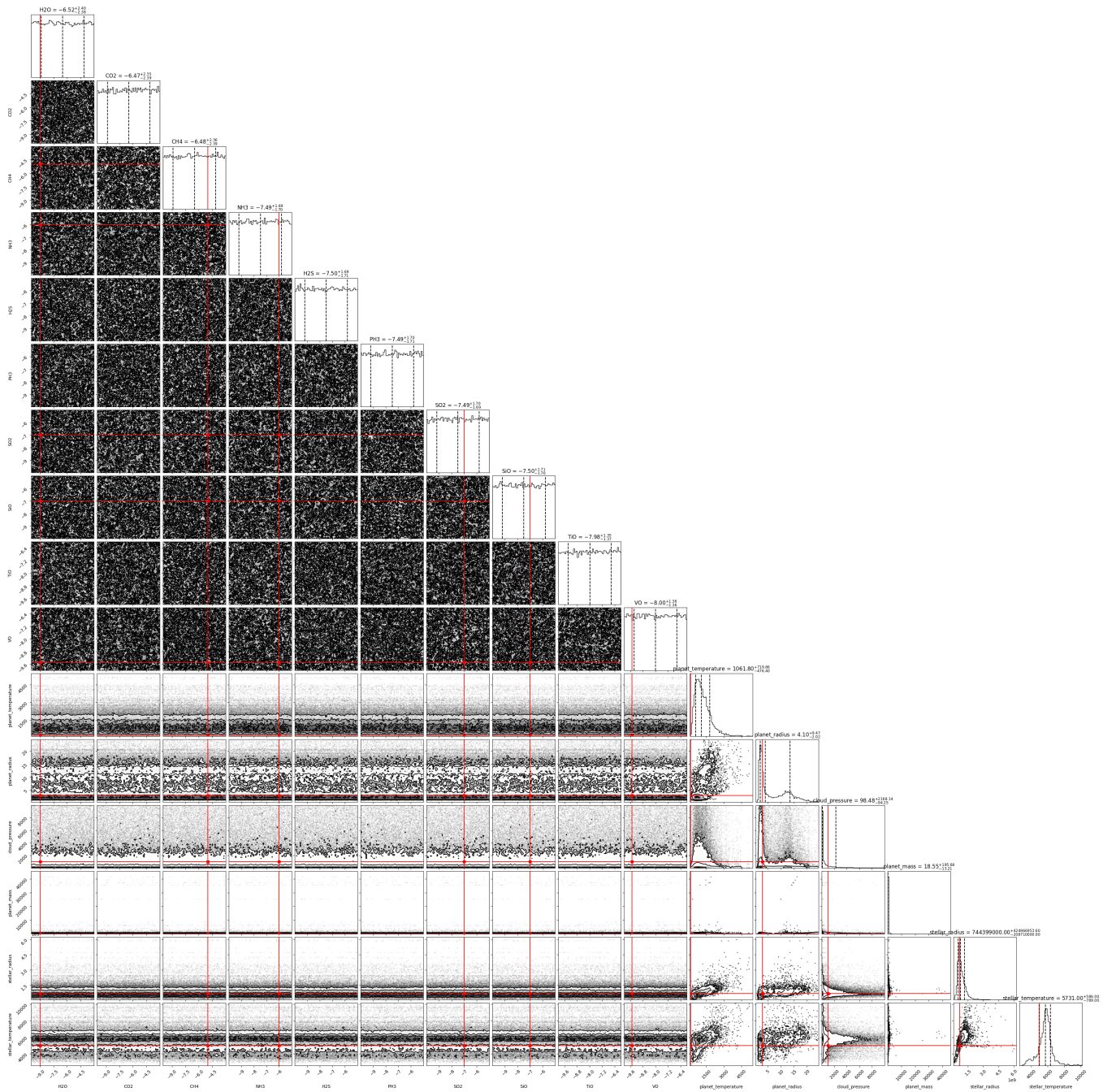


**Figure E2.** The distribution of the simulated data used for this experiment. Shown in red are the values of the specific sample chosen to demonstrate the method.

## APPENDIX F: EXTENDED RETRIEVAL

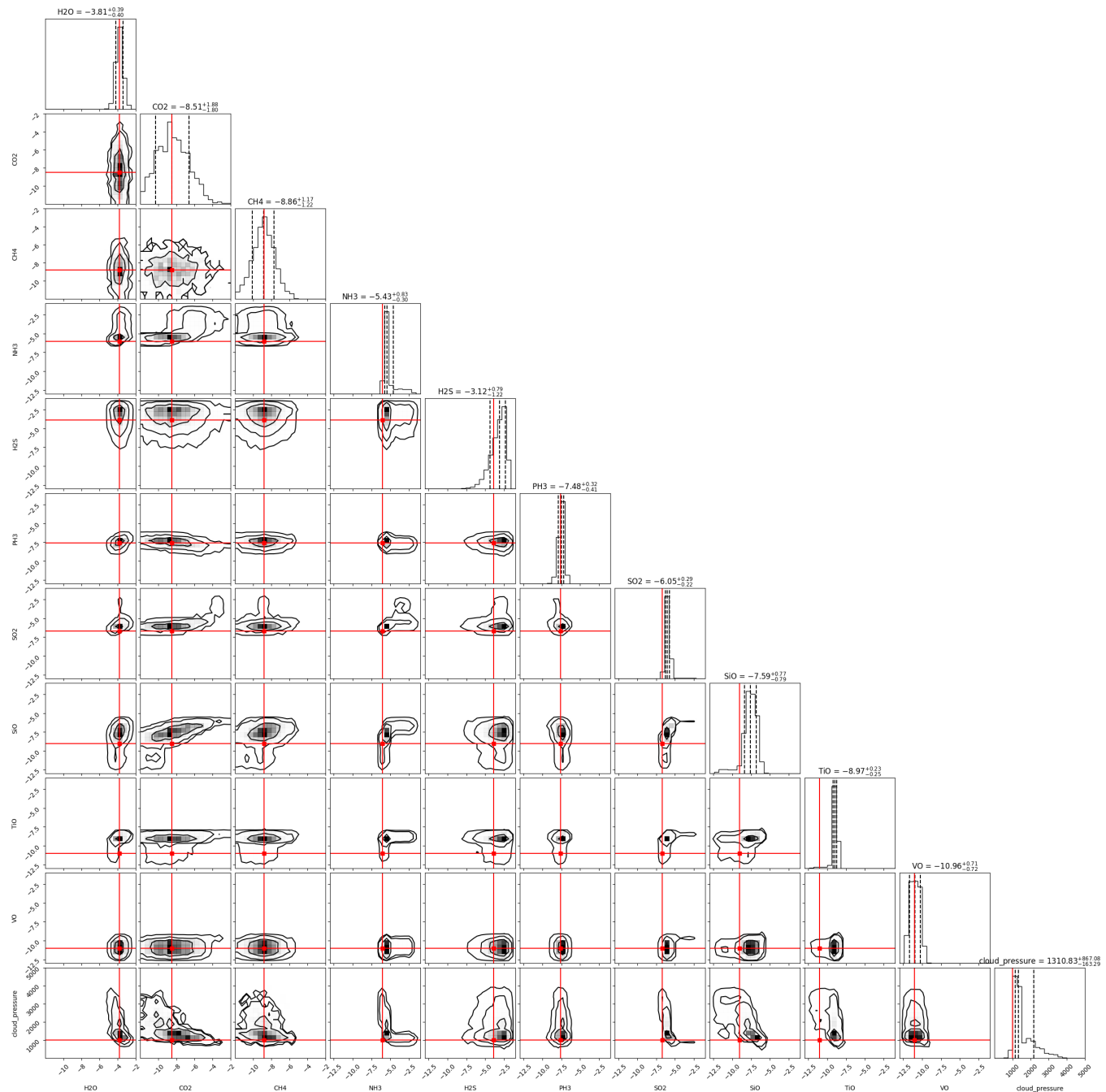


**Figure F1.** Full Retrieval of WASP-107b case study using the machine learning retrieval framework (Clarke et al. 2026). Shown in red are the ground truth values used.